CHALMERS
UNIVERSITY OF TECHNOLOGY

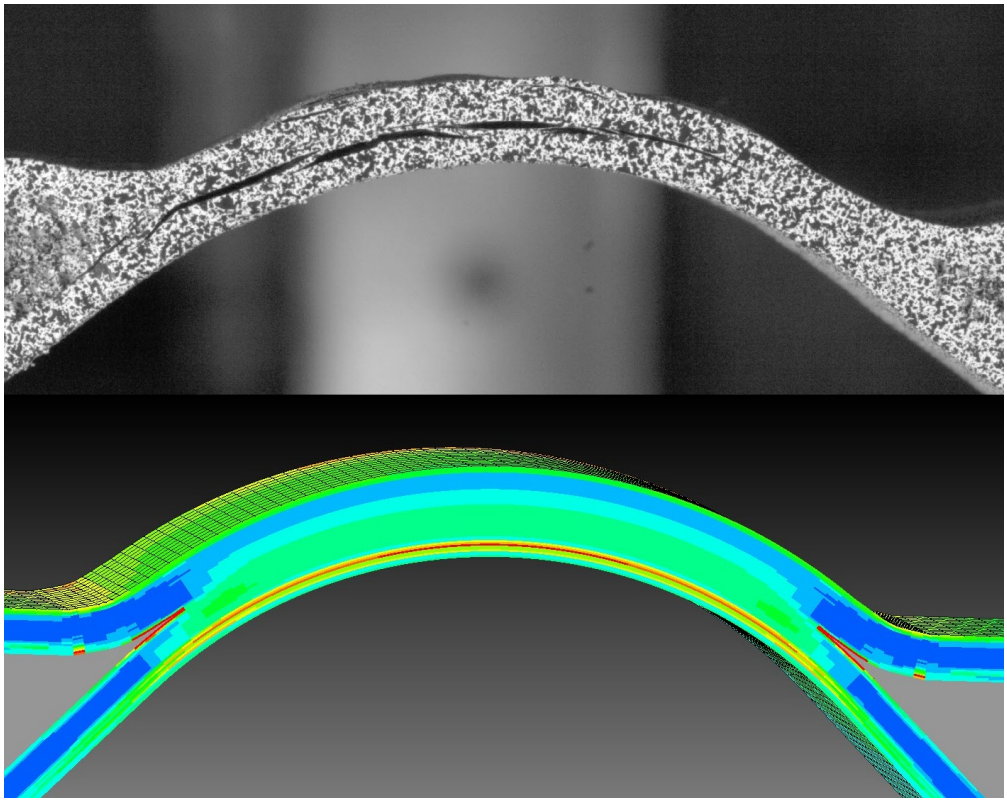

Prediction of interlaminar stress in composite sandwich joints

A method development for Volvo Buses

Love Roos

Department of Industrial and Materials Science
CHALMERS UNIVERSITY OF TECHNOLOGY
Gothenburg, Sweden 2019

MASTER'S THESIS IN APPLIED MECHANICS 2019

Prediction of interlaminar stress in composite sandwich joints

A method development for Volvo Buses

LOVE ROOS

CHALMERS
UNIVERSITY OF TECHNOLOGY

Department of Industrial and Materials Science
Division of Material and Computational Mechanics
CHALMERS UNIVERSITY OF TECHNOLOGY
Gothenburg, Sweden 2019

Prediction of interlaminar stress in composite sandwich joints
A method development for Volvo Buses
LOVE ROOS

Supervisor: David Lantz, Volvo Buses
Supervisor: Erik Marklund, RISE Research Institutes of Sweden
Examiner: Martin Fagerström, Department of Industrial and Materials Science

Master's Thesis in Applied Mechanics 2019
Department of Industrial and Materials Science
Division of Material and Computational Mechanics
Chalmers University of Technology
SE-412 96 Gothenburg
Telephone +46 31 772 1000

Cover: Failure of curved carbon fiber composite beams, in physical testing and numerical simulations.

Typeset in LaTeX
Gothenburg, Sweden 2019

Prediction of interlaminar stress in composite sandwich joints
A method development for Volvo Buses
LOVE ROOS
Department of Industrial and Materials Science
Chalmers University of Technology

Abstract

Volvo Bus Corporation is one of the worlds largest bus manufacturers and has a long history of using traditional construction materials, such as steel and aluminium alloy. In efforts to meet the demands on reduced emissions and maintained passenger capacity, the company has identified curved composite structures as candidates for weight reductions in future vehicles, where traditional materials today are used. To fully take advantage of the anisotropic properties of composite materials in these applications, new simulation methods able to capture the failure behaviour of these structures are needed.

The current study addresses simulation methodologies for capturing the out−of−plane loading and failure behaviour of curved composite structures subjected to bending moments. Previously developed modelling strategies are discussed and a solid element simulation methodology is chosen. A benchmarking of available numerical software using a reference case is performed, where Abaqus is chosen as solver moving forward. Numerical models of curved composite beam structures are constructed, along with a physical testing protocol for verification of the numerical models. A set of failure criteria are presented and implemented in the numerical models.

The methodology development shows that the first hand use solver *MSC Nastran* can not be used with the available pre and post processors for solid element models where orthotropic material models are used. Results from the numerical simulations using Abaqus show that all beam models without a sandwich design, as well as one beam model with a sandwich design, fail in an out−of−plane matrix interface delamination mode. Two further sandwich beam models predict failure in an in−plane matrix mode, subject to transverse tensile loading of 90° plies. The physical testing shows that failure is not initiated in the junction between the foam core and upper/lower laminate facings, and that the numerical models are somewhat accurate but too stiff. The results are discussed and future work based on the developed solid element simulation strategy is suggested.

Keywords: CFRP, NCF, orthotropic, carbon fiber, curved composites, sandwich structures, LaRC05, Abaqus, MSC Nastran

Acknowledgements

This master's thesis has been made possible with support from the Vehicle Strategic Research and Innovation Programme (FFI) 2017-03083, as a collaboration between Volvo Bus Corporation and RISE Research Institutes of Sweden, which are gratefully acknowledged. I would like to express my deepest gratitude to my supervisors, David Lantz and Erik Marklund, who through their enthusiastic and professional support has given me an opportunity to grow as a student. Your help and guidance has been invaluable and I look forwards to our future endeavors within the industry.

I would like thank my examiner, Associate Professor Martin Fagerström, for giving me the opportunity to work on a thesis focusing on lightweight composite structures. Thank you to Doctor Dennis Wilhelmsson, your eager support as a friend and industry professional has been decisive in my choice to pursue a career path as an engineer. Thank you to Professor Leif Asp for providing inspiration and broadening my horizons within the field of composites. I would like to extend my gratitude to Doctor Henrik Molker for selflessly sharing expertise on the matter at hand. Thank you to Camilla Karlsson and all department colleagues at Volvo Bus Corporation, as well as Christopher Cameron and Gaurav Vyas at RISE, for encouragement and professional advice throughout the project.

Love Roos, Gothenburg, June 2019

Contents

Nomenclature and Abbreviations

Abaqus	FE solver
BETA	Pre and post process software provider
CFRP	Carbon Fiber Reinforced Polymers
D6415	ASTM D 6415 standard
DIC	Digital Image Correlation
DoF	Degree of Freedom
ECS	Element Coordinate System
FE	Finite Element
GCS	Global Coordinate System
HDVs	Heavy Duty Vehicles
MSC Nastran	FE solver
NCF205	NCF composite with $205 g/m^2$ areal weight
NCF	Non Crimp Fiber
P100	Divinycell P100 foam
PET	Polyethylene Terephthalate
PN110	Divinycell PN110 foam
QI	Quasi−isotropic
UD	Uni−directional
VBC	Volvo Bus Corporation

List of Figures

List of Tables

1
Introduction

The present chapter gives an introduction to the thesis, presenting Volvo Bus Corporation as a company while addressing the background to the problem at hand. The aim of the thesis is further presented along with a scope and a set of delimitations.

1.1 Background

Volvo Bus Corporation (VBC), a part of Volvo Group, is one of the worlds largest bus manufacturers, producing about 10 000 vehicles yearly while operating on a global market. VBC has a vision of presenting a premium product, being a world leader within sustainable transport solutions and ensuring that end customers reach their destination every day.

One way of contributing to this vision is to develop new vehicles with the aim of reducing fuel consumption, while maintaining passenger capacity and focusing on structural integrity. This can be done by enabling weight reductions on load carrying structures through an introduction of new materials and optimised simulation methodologies. For heavy duty vehicles (HDVs) such as city buses and long distance coaches, reducing the vehicle weight by 100 kg can imply emission reductions of up to 6.9 gCO_2/km [1]. Reducing emissions of greenhouse gases in new vehicles is furthermore a key target of the European Commission climate & energy framework for the year 2030 [2].

An introduction of lightweight materials previously unused in a large scale by VBC, such as Carbon Fiber Reinforced Polymers (CFRP), can facilitate weight reductions with unchanged or improved durability, compared to traditionally used materials such as steel or aluminum [3]. New challenges however arise, with questions on how CFRP materials can be used in the best way to redesign current components, in order to take full advantage of the materials anisotropic nature.

VBC has identified that candidates for weight reduction in future vehicles, using CFRP materials, include curved load carrying components with complex geometries. These components can be composed of flat sandwich sections, with CFRP laminates on top of a core material, joined together with a curved CFRP section without a core. A schematic image of such a structure, where two sandwich panels taper down to a curved laminate without a core, can be seen depicted in Figure 1.1. This type of design utilizes the increased second moment of inertia of the component, obtained through the use of sandwich panels, while reduces the manufacturing complexity, since the foam cores do not have to be cut to fit the curved section.

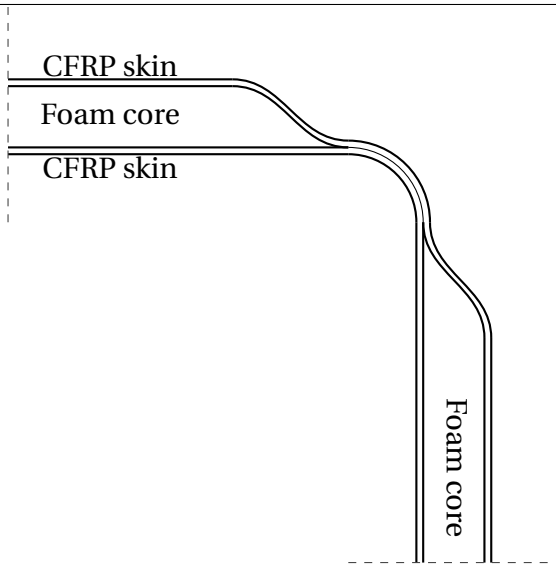

Figure 1.1: Schematic image of sandwich and monolithic cross section in a 90° bend.

1.2 Problem description

Because of the complexity of the structures introduced above, where materials with different properties are used in a curved geometry, careful consideration has to be taken to how modelling is performed to ensure that failure can be predicted in a satisfyingly accurate way. As of today, VBC does not employ a standardised or verified modelling method for failure prediction of curved composite structures. It is thus unknown at what loads these structures may fail, how changes in design parameters may affect failure behaviour and what failure modes that are most likely triggered.

VBC believes that critical parts may consist of either the curved laminate, which can be subjected to large bending moments causing delaminations, or the tapering end of the foam cores with adjacent laminates, which can be affected by manufacturing defects giving stress concentrations. Both these theories are however yet to be proven, and further knowledge on the failure behaviour of the structure is needed. Ensuring that VBC can employ a verified and sufficiently accurate simulation methodology for failure prediction of curved composite structures can thus be crucial to the development of future vehicles, where reduced emissions and maintained passenger capacity are both key features.

1.3 Aim

The aim of this Master's Thesis is to develop, verify and deliver a simulation methodology that sufficiently accurately predicts when and where failure occurs in curved CFRP sandwich sections, subjected to bending moments.

1.4 Scope and limitations

To address the problem at hand and clarify the intentions of the thesis, a scope and set of delimitations are presented below.

The thesis shall present a numerical simulation methodology developed for failure prediction of CFRP sandwich structures with a 90° curve, subjected to bending moments. The methodology and developed models shall account for different geometries, laminate properties, mesh configurations and mechanical properties of constituent materials. Pre, post and solving software used shall be currently available to VBC. An investigation of relevant failure criteria and the possibilities to automate the model generation shall be made. The thesis shall verify results from the numerical simulations through physical testing and discuss possible differences in results. Only the foam core and laminates in closest proximity to the curved section will be evaluated. The verification methodology, containing a description of coupon manufacturing and test rig setup, shall further be provided.

The scope of the thesis is delimited by the time available in the present course, with 30 university credits available, corresponding to 20 weeks of working time. The thesis will only evaluate curved beams with similar geometrical configuration as that depicted in Figure 1.1, where the constituent material properties are known. Only Non Crimp Fiber (NCF) type composite and closed cell foam core materials will be evaluated for failure and only first ply failure, not progressive damage, will be evaluated for the NCF material. The scope of the physical testing will be delimited by availability of material at the time of coupon manufacturing as well as operator working time.

2

Theory

The present chapter describes the theoretical background relevant to the study. Properties of orthotropic NCF composites are presented along with failure criteria and a description of an ASTM standard for destructive physical testing of curved composite structures.

2.1 Composite laminates

Composite materials consisting of long fiber CFRP sheets can be made in an almost indefinite number of configurations, with strength and stiffness properties dependent on constituents materials, fiber volume fraction, manufacturing methods and other parameters. A layered composite sheet is commonly called a *laminate* and is a composition of several thinner *lamina*, also called plies. The orientation of each lamina, which is consistent with its main fiber direction, is defined by the plane spanned by the laminate and the rotation angle about the out-of-plane axis. Figure 2.1 displays a schematic image of a laminate consisting of eight plies, with symmetry about the mid-plane. This configuration is said to be a $[90/90/0/0]_s$ layup, with 0° plies oriented along the x-axis and 90° plies rotated in a positive angle about the out-of-plane z-axis.

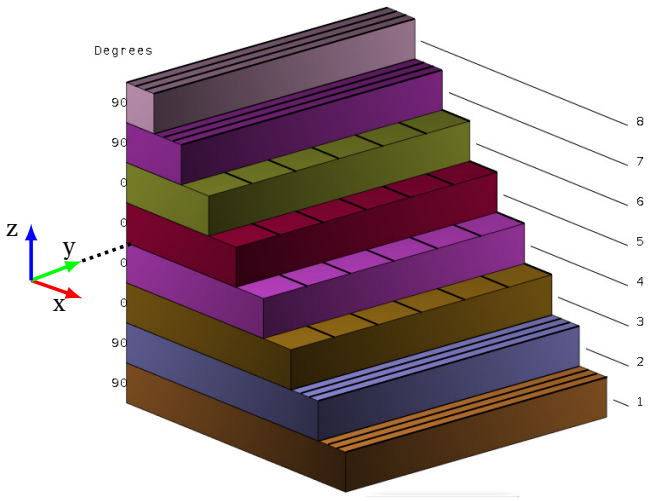

Figure 2.1: Schematic image of a laminate with a $[90/90/0/0]_s$ layup.

2.2 Orthotropic properties

Governed by the generalized Hooke's law, CFRP materials are anisotropic in stress-strain response, meaning that they have different properties in different directions. While individual carbon fibers by themselves are said to have transversely isotropic properties, manufactured CFRP materials may posses orthotropic properties. This means that the materials have three orthogonal symmetry planes for which the elastic response is independent of normal vector sign. In other words, reversing the sign for the surface normals of the X_1X_2, X_2X_3 and X_1X_3-planes does not change the elastic response for the material.

With a starting point in Hooke's generalized law, taking symmetry in stress and strain for anisotropic materials as well as thermodynamic arguments into account, the stress tensor for orthotropic materials can be written as Equation (2.1), in Voigt notation.

$$\begin{bmatrix} \sigma_x \\ \sigma_y \\ \sigma_z \\ \tau_{yz} \\ \tau_{xz} \\ \tau_{xy} \end{bmatrix} = \begin{bmatrix} C_{11} & C_{12} & C_{13} & 0 & 0 & 0 \\ C_{12} & C_{22} & C_{23} & 0 & 0 & 0 \\ C_{13} & C_{23} & C_{33} & 0 & 0 & 0 \\ 0 & 0 & 0 & C_{44} & 0 & 0 \\ 0 & 0 & 0 & 0 & C_{55} & 0 \\ 0 & 0 & 0 & 0 & 0 & C_{66} \end{bmatrix} \begin{bmatrix} \epsilon_x \\ \epsilon_y \\ \epsilon_z \\ \gamma_{yz} \\ \gamma_{xz} \\ \gamma_{xy} \end{bmatrix} \tag{2.1}$$

With the constitutive relation between stress and strain for the three symmetry planes being independent on normal direction of the planes, nine independent elastic parameters are thus needed to describe the constitutive relationship, $C_{11}, C_{22}, ..., C_{66}$ and C_{12}, C_{13}, C_{23} [4]. In practice, this means that Young's moduli, shear moduli and Poisson's ratios are needed in all three directions to model composite materials with orthotropic properties. As an example, Figure 2.2 displays a test volume of an orthotropic material where Young's modulus is different in all three directions.

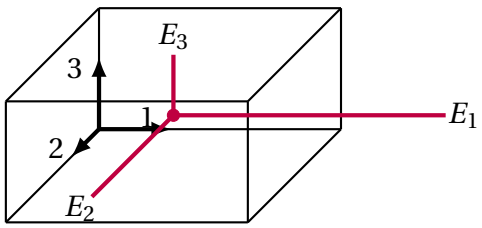

Figure 2.2: Orthotropic properties, with different Young's modulus in all three directions.

2.3 Woven fabrics and the effect of crimp

Among CFRP materials that are commonly used in the industry, we find *woven fabrics*. These materials include carbon fiber tows, which consist of bundled individual carbon fibers, interlaced to each other in either a 2D or 3D-pattern. For a weaving process in 2D, two sets of tows are interlaced perpendicular to each other to create the desired pattern. Tows that

run in the length-wise direction of the fabric are called *warp* tows, while the tows in the transverse direction are called *weft* tows. These can be either pre-impregnated by resin or kept dry during the weaving process. [5]. Woven fabrics are often used because they offer simplicity in the production process, with regard to draping of complex geometries. This simplicity does however come at the cost of fiber misalignment.

Since traditional CFRP fabrics with a woven structure involve interlacing of warp and weft tows, fiber misalignment and crimp is introduced in the material architecture. Crimp is defined as the quotient between the length of the tow in the fabric and the length of the fabric itself, as described by Equation (2.2) [6]. Fiber misalignment adversely affects both the in-plane strength and stiffness properties of the material [7], mainly affecting the longitudinal compression strength due to formations of kink-bend initiations [8].

$$C = \frac{l_t - l_f}{l_f} \quad where \quad \begin{cases} l_t \text{ is the tow length} \\ l_f \text{ is the fabric length} \end{cases} \tag{2.2}$$

2.4 Non-Crimp Fiber materials

Similarly to woven fabrics, Non-Crimp Fiber (NCF) materials are composed of fiber tows, but unlike regular woven fabrics, NCF materials are made in such a way that the fiber tows do not interlace. Fiber misalignment is thus minimized and strength as well as stiffness properties may be kept higher, compared to a traditional woven fabrics. To hold the material together, tows are stitched through the thickness by threads in the warp and/or weft directions. These threads are often made of glass fiber or thermoplastic materials. An industrially used NCF can be seen depicted in Figure 2.3. Here, the warp-weft configuration is of uni-weave type, meaning that all fiber tows are oriented in the 1-direction of the ply [9].

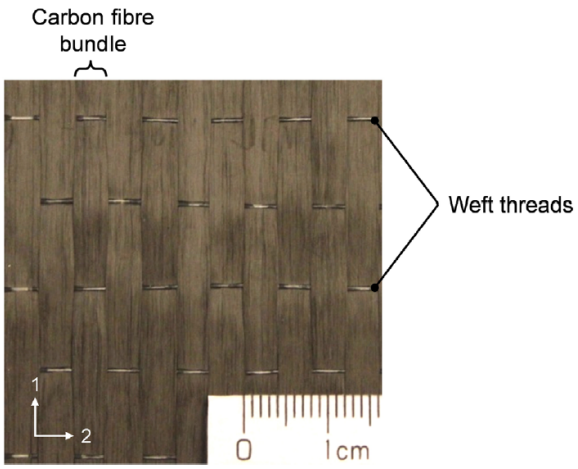

Figure 2.3: Uni-weave NCF bulk material, picture courtesy of Bru. et al. [9].

NCF composites are found to have orthotropic properties, with strength and stiffness differing from each other in the in-plane transverse and out-of-plane directions. Studies have shown that the out-of-plane strength in tension for NCF composites can be approximately

half of the in-plane transverse strength [10], it can however be argued that this is dependent on manufacturing methods, the amount of crimp or other factors. Even though the amount of crimp is kept low in NCF composites, yarn stitching may disturb the fiber alignment and thus affect compression strength in an adverse way [8].

The NCF composite evaluated in the current study is a uni-weave NCF with of 205 g/m^2 areal weight. The bundles are held together by glass/polyamide yarns and during manufacturing infused with Huntsman LY556 epoxy resin. This material, hereinafter called NCF205, is well characterized by experimental methods, with respect to strength and stiffness properties in all three directions [9]. NCF205 is furthermore subject to several recent studies ([8], [11]) and is currently available to VBC and RISE for physical testing purposes. Experimentally determined elastic and strength properties for NCF205 can be found in Table 2.1 and 2.2 respectively.

Table 2.1: Elastic properties of NCF205 [9].
* parameters calculated as averages of tension and compression

$E^*_{11,205}$ GPa	$E^*_{22,205}$ GPa	$E^*_{33,205}$ GPa	$G_{12,205}$ GPa	$G_{13,205}$ GPa	$G_{23,205}$ GPa	$\nu_{12,205}$ -	$\nu_{13,205}$ -	$\nu_{32,205}$ -
136.0	9.2	8.0	4.3	3.7	2.8	0.29	0.29	0.43

Table 2.2: Strength properties of NCF205 [9].
* conservative choice between monotonic and cyclic loads.
** assumption based on S_{13}.

$X_{T,205}$ MPa	$X_{C,205}$ MPa	$Y_{T,205}$ MPa	$Y_{C,205}$ MPa	$Z_{T,205}$ MPa	$Z_{C,205}$ MPa	$S^*_{12,205}$ MPa	$S^*_{13,205}$ MPa	$S^{**}_{23,205}$ MPa	$\alpha_{0,205}$ deg
1787	631	29.2	130	14.7	203	73	53.7	53.7	62

2.5 Sandwich constructions and foam materials

The use of sandwich structures is not an entirely new feature in the heavy duty vehicles industry, load carrying panels are currently used in both buses and trucks, in various configurations. Sandwich structures with glass or carbon fiber reinforced plastics used as face sheet are furthermore common in similar industries, such as the sports, wind power and defence industries [12]. The advantage of using sandwich structures in heavy duty vehicles such as buses, is the ability to construct relatively stiff components without the weight penalty of a fully homogeneous material, enabling improved passenger capacity or reduced emissions [1].

Core materials for sandwich structures come in four different types; corrugated, honeycomb, balsa wood and cellular foam [12], all which have different advantages and disadvantages. The current study focuses on cellular foams with closed cell structures. Closed cell polyethylene terephthalate (PET) foams, such as Divinycell P100, are shapeable by hot-cutting or milling, resist water penetration due to the cell structure and provide better insu-

lation than other core types, such as honeycomb. The insulating properties give multifunctionality to load carrying components and thus offer possibilities in weight reductions. P100 further meet the required fire, smoke and toxicity demands for use in buses [12], [13]. The drawback of cellular foams, in comparison to corrugated or honeycomb core materials, is lower mechanical properties.

Materials with similar closed cell structure as P100 act linear elastic in stress-strain response up to $2-4\%$ engineering strain, while subjected to compressive loading. Past the elastic region, and under quasi-static loading conditions, stress response may plateau up to approximately 40% engineering strain [14], after which a progressive densification and stress increase takes place. The micro mechanics of closed cell foam failure include buckling of cell walls, formation of plastic hinges and other non-uniform phenomena [15]. Size dependency for compressive modulus has further been observed, with larger cross sections accounting for higher modulus [16].

Modelling of the stress response in closed cell foam after the yield point, especially in the densification range, thus require detailed information on load rate dependency for the material and may further require computationally heavy simulation methods, such as Representative Volume Element analysis. Results in this region should therefore be interpreted with caution [16].

Mechanical properties for P100 representing the manufacturers minimum guaranteed quantities are given in Table 2.3. Young' modulus and Poisson's ratio marked by an asterisk represent values used in the numerical simulations due to an input error.

Table 2.3: Material properties of P100 foam [13].
* Used in numerical simulations.

E_{P100} MPa	E^*_{P100} MPa	ν_{P100} –	ν^*_{P100} –	G_{P100} MPa	ρ_{P100} kg/m^3	$\sigma_{u,C,P100}$ MPa	$\sigma_{u,T,P100}$ MPa	$\sigma_{u,S,P100}$ MPa
60	58.82	0.363	0.337	22	110	1.1	1.35	0.69

The mechanical properties for Divinycell PN115 (PN115), which is the foam used for manufacturing of the sandwich coupons, are given in Table 2.4. As described in Section 3.5.1, this material is chosen due to a limited availability of P100 at the time of coupon manufacturing. PN115 is similarly to P100 a PET-based foam with closed cell structure.

Table 2.4: Material properties of Divinycell PN115 foam [17].

E_{PN115} MPa	G_{PN115} MPa	ρ_{PN115} kg/m^3	$\sigma_{u,C,PN115}$ MPa	$\sigma_{u,S,PN115}$ MPa
85	23	115	1.35	0.8

2.6 Failure criteria for the structure

The curved structures subject to the current study consist of sections with different elastic properties, being the foam cores that are assumed isotropic, as well as the NCF laminates that are orthotropic. Different failure criteria will be applied to these parts, respectively. The entire structure is assumed to fail on the first load step in which either a foam or NCF criteria is exceeded. Sections 2.7 and 2.8 address relevant failure criteria for isotropic foam type materials and NCF laminates, respectively.

2.7 Failure criteria for foam materials

Failure prediction of closed cell foam materials is a complex matter, since high fidelity predictions require experimentally determined information about the rate dependency of the constitutive relation within the plastic region. To simplify the modelling procedure in the present study, the foam is assumed to be *isotropic* in the elastic region, with *perfectly plastic* behaviour in the plastic region. An elastic-perfectly plastic modelling approach is found to be the method of choice in similar studies, where sandwich beams are subjected to bending moment in quasi-static load conditions [14].

2.7.1 Von Mises yield criterion

The von Mises stress equivalence $\sigma_{e,vM}$ is based on the second invariant of the deviatoric stress tensor, meaning that it is independent of hydrostatic pressure [18]. In the present study, the choice is made to evaluate von Mises effective stress against the minimum guaranteed shear stress limit $\sigma^*_{u,S}$, due to lack of material data. Failure is thus considered to be present when the von Mises equivalent stress exceeds the shear stress limit.

$$\begin{aligned}\sigma_{e,vM} = \frac{1}{\sqrt{2}}\big[(\sigma_{xx}-\sigma_{yy})^2 + (\sigma_{yy}-\sigma_{zz})^2 + (\sigma_{zz}-\sigma_{xx})^2 + \\ 6\tau_{yz}^2 + 6\tau_{zx}^2 + 6\tau_{xy}^2\big]^{1/2} \quad \leq \quad \sigma^*_{u,S}\end{aligned} \tag{2.3}$$

2.7.2 The yield criterion for isotropic materials, accounting for the effect of hydrostatic pressure

The yield criterion for isotropic materials, accounting for the effect of hydrostatic pressure, hereinafter called the Hydrostatic Criterion (HC), is originally developed for soil, but also used for polymers and polymeric foams [19]. The criteria takes the effect of hydrostatic pressure on yield strength into account based on experimental results, and assumes a linear combination of von Mises equivalent stress and hydrostatic pressure to describe when yielding takes place. The hydrostatic pressure can be written as Equation (2.4).

$$\sigma_m = \frac{\sigma_{xx}+\sigma_{yy}+\sigma_{zz}}{3} \tag{2.4}$$

Using von Mises equivalent stress of Equation (2.3) and the hydrostatic pressure of Equation

(2.4), the Hydrostatic Criterion can be formulated as Equation (2.5). Failure is considered to be present when the equation reaches unity. Here, A and B are constants that can be written in terms of known strength parameters, where $\sigma^*_{u,T}$ is the ultimate tensile strength of the material and $\sigma^*_{u,C}$ is the compressive strength.

$$\sigma_{HC} = A\,\sigma_{e,vM} + B3\sigma_m \leq 1 \tag{2.5}$$

$$A = \frac{\sigma^*_{u,T} + \sigma^*_{u,C}}{2\,\sigma^*_{u,T}\,\sigma^*_{u,C}}, \qquad B = \frac{\sigma^*_{u,C} - \sigma^*_{u,T}}{2\,\sigma^*_{u,T}\,\sigma^*_{u,C}} \tag{2.6}$$

2.8 Failure criteria for NCF composites

Failure criteria for composite laminates are most often evaluated *within* each lamina, with the stress state considered in terms of the local coordinates L, T and TT, corresponding to the main fiber, in-plane transverse and out-of-plane directions respectively. Normally only first ply failure is considered, meaning that the first sign of a deterioration in load carrying capability, through triggering of a failure criteria, is interpreted as a design limit for the laminate. This approach implies that the laminate is considered to have failed at a load level in which it may not yet have lost a considerable amount of its load bearing capability. Predictions are thus, under some circumstances, conservative given that a relevant failure criteria is used.

An alternative approach when evaluating failure of a laminate is to apply progressive damage modelling after first ply failure, by discounting some or all ply properties after the failure criteria is triggered. This method is dependent on what specific failure criteria that is implemented and in order for the method to be accurate, physically based failure criteria that are able to capture different failure modes has to be used [4]. Because of the complexity of this approach, and since VBC currently wish to model failure of composites conservatively, progressive failure modelling is not performed in the present study.

Various well documented failure criteria are currently available to VBC, all of which have different advantages and disadvantages with respect to prediction accuracy, verification possibilities and implementation complexity. Classic criteria for anisotropic composite materials, such as Maximum Stress or Tsai-Wu, are easy to use due to the level of software implementation and the availability of reference cases, which can be used for model verification. These criteria are however developed for uni-directional (UD) fiber composites under the assumption of transverse isotropy, a special case of orthotropy, and thus not fully suited for NCF composites where the out-of-plane and in-plane properties are dissimilar. Maximum Stress does furthermore not take load interaction into consideration, which makes it non-conservative, while Tsai-Wu require experimentally determined parameters, which may be cumbersome to calibrate [4], [20].

More advanced failure criteria are based on experimental testing and take load interaction into account, while describing failure by different modes, both on an intra- and interlaminar level. These include LaRC05 [21] and the Orthotropic Criteria for Transverse Failure of NCF-reinforced Composites [22], presented below.

2.8.1 Maximum Stress

The Maximum Stress criteria is a set of equations normally used to evaluate failure of transversely isotropic UD lamina under the assumption of plane stress. The criteria can be expanded to 3D form, as presented in Equation (2.7), and used to evaluate failure of orthotropic materials, such as NCF composites. This require that the full 3D stress state for the lamina is known, as well as the strength parameters of the material. The criteria states that intralaminar failure occur when the stress in one of the three local ply directions exceed the corresponding ultimate strength, in tension, compression or shear. Load interaction or the effect of physical failure modes, such as kink-bend failure during in-plane compression, are not taken into account. The criteria is thus non-conservative, however easy to implement if all strength parameters for the material are known [4].

$$\begin{cases} -X_C < \sigma_L < X_T \\ -Y_C < \sigma_T < Y_T \\ -Z_C < \sigma_{TT} < Z_T \\ |\tau_{LT}| < S_{12} \\ |\tau_{LTT}| < S_{13} \\ |\tau_{TTT}| < S_{23} \end{cases} \tag{2.7}$$

2.8.2 Tsai-Wu for orthotropic properties

The Tsai-Wu failure criteria is developed for material characterization of, and design work with, anisotropic materials [20]. The criteria employs a basic assumption that there is a failure surface in the stress-space that follows an ellipsoidal shape, which can be described by a linear combination of stress terms. This assumption is based on a purely mathematical approach, where load interaction is taken into account through curve-fitting the failure surface, without regard to physical failure modes. The criteria is normally more conservative than Maximum Stress, but may in certain situations give rise to unphysical strength prediction [4]. The failure criteria can be written as Equation (2.8), for orthotropic materials.

Failure is said to occur when the left hand side ≥ 1.

$$\begin{aligned} &\frac{\sigma_L^2}{X_T X_C} + \frac{\sigma_T^2}{Y_T Y_C} + \frac{\sigma_{TT}^2}{Z_T Z_C} + \frac{\tau_{LT}^2}{S_{12}^2} + \frac{\tau_{LTT}^2}{S_{13}^2} + \frac{\tau_{TTT}^2}{S_{23}^2} + \\ &(\frac{1}{X_T} - \frac{1}{X_C})\sigma_L + (\frac{1}{Y_T} - \frac{1}{Y_C})\sigma_T + (\frac{1}{Z_T} - \frac{1}{Z_C})\sigma_{TT} + \\ &2F_{12}\sigma_L\sigma_T + 2F_{13}\sigma_L\sigma_{TT} + 2F_{23}\sigma_T\sigma_{TT} \quad < \quad 1 \end{aligned} \tag{2.8}$$

Here, the parameters F_{12}, F_{13} and F_{23} influence both the slenderness ratio and inclination of the ellipsoid axes [4]. In theory, these parameters can be experimentally determined by imposing a purely biaxial stress state, as described by Equation (2.9) for F_{12}, where parameters F_{13} and F_{23} follow an analogue relation. At the onset of failure, biaxial stress state for F_{12} implies that $\sigma_1 = \sigma_2 = \sigma_{biax}$ while $\sigma_3 = \tau_{12} = \tau_{13} = \tau_{23} = 0$.

$$F_{12} = \frac{1}{2\sigma_{biax}^2}\left[1 - \sigma_{biax}\left(\frac{1}{X_T} - \frac{1}{X_C} + \frac{1}{Y_T} - \frac{1}{Y_C}\right) - \sigma_{biax}^2\left(\frac{1}{X_T X_C} + \frac{1}{Y_T Y_C}\right)\right] \tag{2.9}$$

In practice, this load case is however nearly impossible to achieve and an alternative approach to finding F_{12} is needed. By assuming the parameter according to the relation described by Equation (2.10), and letting F_{13} and F_{23} follow the same relation, the Tsai-Wu criteria can be implemented.

$$F_{12} = \frac{1}{\sqrt{X_T X_C Y_T Y_C}} \tag{2.10}$$

2.8.3 LaRC05

The LaRC05 failure criteria, developed in 2012 and an iteration of earlier experimentally developed criteria [23], predicts intralaminar failure by three physical modes; intralaminar matrix failure, fiber tensile failure and fiber kinking. LaRC05 require more material parameters than Maximum Stress or Tsai-Wu, but in return yields a greater amount of information about the predicted failure, with mode type as well as intralaminar fracture plane angle α among the output [22]. Failure within the ply is said to occur when one of the failure indices in the criteria ≥ 1. All three indices in the criteria take *in-situ* effects into account, meaning that transverse tensile strength as well as longitudinal and transverse shear strengths are considered to be higher for a lamina that is located between plies of other fiber orientations. For transversely isotropic UD composites however, only the transverse shear strength is adjusted for in-situ effects [23], [21].

Matrix failure

The index of *matrix failure* in LaRC05 is defined by Equation (2.11).

$$FI_M = \left(\frac{\tau_T}{S_T^{is} - \eta_T \sigma_N}\right)^2 + \left(\frac{\tau_L}{S_L^{is} - \eta_L \sigma_N}\right)^2 + \left(\frac{\langle \sigma_N \rangle_+}{Y_T^{is}}\right)^2 \tag{2.11}$$

Here, superscript *is* signifies in-situ strengths of the ply. The shear forces τ_T, τ_L and normal stress σ_N are defined by Equation (2.12) and can be seen depicted on the potential failure surface in Figure 2.4. The figure further displays the fracture plane angle α, which is defined as the positive rotation from the *13*-plane about the main fiber direction, that maximizes any of the three failure indices.

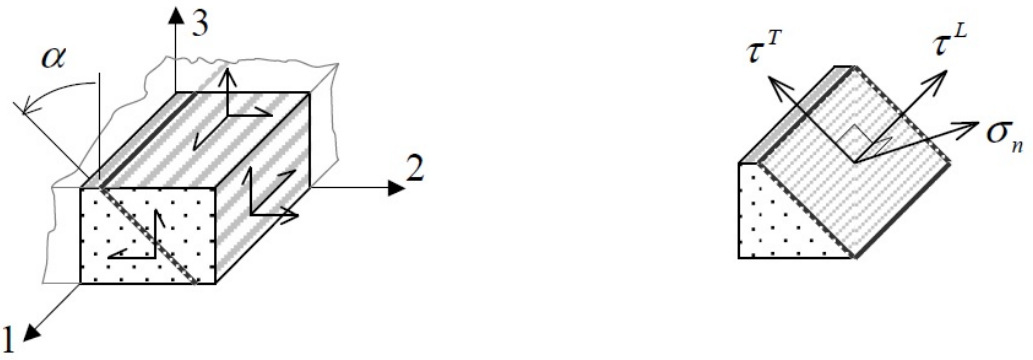

Figure 2.4: Fracture plane angle α and shear as well as normal forces on the plane, courtesy of Pinho. et al [23].

The last term of Equation (2.18) contains the positive normal stress contribution $\langle \sigma_N \rangle_+$, defined using the Macauley bracket of Equation (2.13). The physical interpretation to this term is that only tensile normal stress open potential cracks, or in other words that compressive normal stress closes potential cracks. The normal stress σ_N can also be found in the denominator of the first two terms where it acts as a friction contribution, increasing transverse and longitudinal strength in compression if $\sigma_N < 0$.

$$\begin{cases} \sigma_N = & \frac{\sigma_2+\sigma_3}{2} + \frac{\sigma_2-\sigma_3}{2} cos(2\alpha) + \tau_{23} \\ \tau_T = & -\frac{\sigma_2-\sigma_3}{2} cos(2\alpha) sin(2\alpha) + \tau_{23} cos(2\alpha) \\ \tau_L = & \tau_{12} cos(\alpha) + \tau_{31} sin(\alpha) \\ \alpha = & [-\pi, \pi] \end{cases} \tag{2.12}$$

$$\langle \sigma_N \rangle_+ = \begin{cases} \sigma_N & \text{if x} > 0 \\ 0 & \text{if x} \leq 0 \end{cases} \tag{2.13}$$

Fiber tensile failure

The index of *fiber tensile failure* in LaRC05 stems from the Maximum Stress criteria, where X_T is the design limit for ply subject to tensile loading in the main fiber direction. The fracture plane of this failure mode is assumed to be perpendicular to the main fiber direction of the ply [21].

$$FI_{FT} = \frac{\langle \sigma_1 \rangle_+}{X_T} \tag{2.14}$$

Fiber kinking/splitting

The index of *fiber kinking* in LaRC05 is defined by Equation (2.15), which also represents a fiber splitting index FI_{SPLIT}. Splitting is assumed to occur for compressive loading along the misaligned fibres if $\sigma_1 \geq -X_C/2$, while kinking is assumed to occur if $\sigma_1 < -X_C/2$. Kinking failure is arguably one of the least understood failure mechanisms for long fiber composite materials, even though kink bands commonly are observed in materials that have failed due to compressive loading. LaRC05 assumes that kinking failure follows local matrix failure in shear-dominated regions. Also in this failure index, in-situ effects on ply strength are taken into account. [21].

$$FI_{KINK} = FI_{SPLIT} = \left(\frac{\tau_{23}^m}{S_T^{is} - \eta_T \sigma_2^m}\right)^2 + \left(\frac{\tau_{12}^m}{S_L^{is} - \eta_L \sigma_2^m}\right)^2 + \left(\frac{\langle \sigma_2^m \rangle_+}{Y_T^{is}}\right)^2 \tag{2.15}$$

Constituents of the failure index equation signified by the superscript m are calculated in what is said to be a misalignment frame, in which a coordinate transformation has been made so that the 1-direction of the stress tensor is parallel to the misaligned fibers [22]. The full coordinate system transformations can be found in Reference [21].

2.8.4 Orthotropic Criteria for transverse failure of NCF-reinforced composites

The Orthotropic Criteria for transverse failure of NCF-reinforced composites, hereinafter called *the Orthotropic Criteria* or in short *LaRC OC*, is developed to address the lack of experimentally and physically based failure criteria for orthotropic materials, such as NCF composites. The Orthotropic Criteria is based on work by previous authors and adapts two failure indices from the LaRC05 criteria, being the *fibre tensile* and *fiber kinking/splitting* indices for transversely isotropic UD composites, as described by Equations (2.14) and (2.15) respectively. The criteria further suggests three new indices to account for the 3D properties of orthotropic NCF composites. [22]

Assumptions from LaRC05, stating that the transverse shear strength S_T, tensile strength Y_T and compressive strength Y_C are dependent of the pure transverse compression angle α_0, not the fracture plane angle α, are kept in the Orthotropic Criteria. The assumption that in-situ effects are present is also maintained, however limited to the effects for UD lamina. The Orthotropic Criteria further considers the out-of-plane strength for a potential fracture plane angle $\alpha = \pi$. Failure predicted by the criteria is said to occur when the largest of the five indices ≥ 1 [22].

Matrix interface failure

The first index introduced is *matrix interface failure*, evaluated when the fracture plane angle $\alpha = \pi$. This aims to capture interbundle failure of the matrix between NCF plies, caused by the forces acting on the matrix interface and the lower out-of-plane strength in tension Z_T, of orthotropic NCF composites.

$$FI_{M,MI} = \left(\frac{\tau_{T,MI}}{S_T - \eta_T \sigma_N}\right)^2 + \left(\frac{\tau_{L,MI}}{S_L - \eta_L \sigma_N}\right)^2 + \left(\frac{\langle \sigma_N \rangle_+}{Z_T}\right)^2 \tag{2.16}$$

The normal stress in the last term of the equation is similarly to Equation (2.11) only evaluated in tension, however against the out-of-plane strength in tension, Z_T.

Bundle failure

The second failure index introduced is *bundle failure*, which aims to capture failure at other potential fracture planes than $\alpha = \pi$. This index is a slight adaptation from the matrix interface mode of Equation (2.16). Here, only the in-situ effects for UD composites are considered. Stress components are evaluated on the potential fracture plane, with shear components signified by subscript B and the normal component yet again only considered in tension [22].

$$FI_{M,B} = \left(\frac{\tau_{T,B}}{S_T - \eta_T \sigma_N}\right)^2 + \left(\frac{\tau_{L,B}}{S_L - \eta_L \sigma_N}\right)^2 + \left(\frac{\langle \sigma_N \rangle_+}{Y_T}\right)^2 \tag{2.17}$$

In-plane matrix failure

The third index describes in-plane matrix failure, and is taken as the maximum of Equations (2.16) and (2.17).

$$FI_M = max\left(FI_{M,MI}, FI_{M,B}\right) \tag{2.18}$$

2.9 Testing standard, ASTM D 6415/D 6415M -06a

The ASTM *D 6415* standard (D6415) defines a testing methodology for determining the out-of-plane strength of fiber-reinforced composite beams, where the tested structure consist of two straight legs connected by a 90° bend. The standard is valid for testing of long fiber composite materials of both unidirectional and woven fabric type (e.g. NCF). Any layup may be used, as long as coupons can be manufactured in accordance to the specified dimensions. Loading is imposed on the structure through a force or displacement controlled four point bending rig, with parallel and friction free rollers. A permanent force versus displacement recording shall take place during the full testing sequence. For UD coupons, the standard states that failure is likely to be initiated in an out-of-plane mode, while it for non-UD coupons may be initiated in other modes, due to edge effects or matrix imperfections [24].

The most relevant rig and coupon dimensions specified by the test standard can be found in Table 2.5.

Table 2.5: Rig and coupon dimensions from the ASTM standard [24].

Specimen				**Rig**		
L_{leg} mm	$t_{laminate}$ mm	r_{inner} mm	w mm	l_t mm	l_b mm	d_{roller} mm
≥ 90	2-12 ± 1	6.4	25± 1	75 ± 2	100 ± 2	10

The standard further states that five or more specimen of each coupon type shall be tested to assure that statistically significant data is obtained. Common error sources, known to cause data scatter among the recorded material, are stated as poor material fabrication, lack of fiber alignment and improper test rig machining. A special caution is further made to the test methods sensitivity to matrix voids within the laminate [24].

3
Methods

The following chapter describes the methodology of the study, for which the basic outline can be seen in Figure 3.1. The contents of the chapter reflects the fact that it is not only important for VBC to predict failure of curved composite structures, but also to obtain an understanding of how the available numerical software can be used in this process.

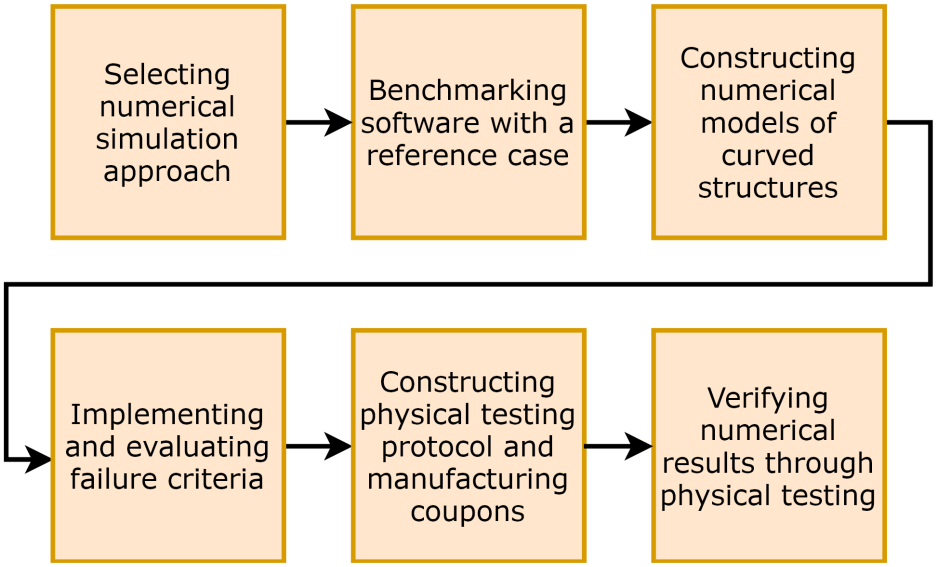

Figure 3.1: Methodology outline.

3.1 Selecting numerical simulation approach

VBC currently employs a modelling strategy for isotropic materials where commonality between different virtual verification disciplines, such as durability and crash safety, is strived after. Here, the first hand use software here includes pre and post processors within the *BETA* package and the Finite Element (FE) solver *MSC Nastran*. The second hand alternative as an FE solver is *Abaqus*.

Modelling of complete buses at VBC is usually performed using a linear shell element approach with standardised mesh settings, since this provides commonality while giving a good balance between accuracy and computational cost. These models do however not predict the transverse stress, which as discussed in Section 2.4 may be critical for curved NCF composite structures.

Other modelling techniques, able to predict the out−of−plane stress state, are however in existence. One approach is to post process in-plane stress results from second order shell models, to get an approximation of the out-of-plane stress state [25]. While this method is more than 20 years old, and has been used in recent studies [11], it is at the present time not implemented in the FE solvers available to VBC. Another approach is to use an adaptive node-based sub modelling technique, in which displacement results are mapped from a global shell model to local sub models consisting of solid elements, where the full stress tensor can be resolved. This technique has been used in recent studies of isotropic materials and is implemented in current versions of *Abaqus*, but requires that the position of the critical areas subject to evaluation is known [26]. It is further possible to fully employ a solid element approach for the complete structure, disregarding sub modelling techniques. This method is currently implemented at VBC for certain isotropic materials, but comes at a considerable computational cost and may not be practical for large scale models where thin composite laminates are used.

Considering these limitations, a solid element approach can however, if implemented correctly, be used to predict failure of curved structures as well as provide a starting point for future work with sub modelling techniques. Because of this, a solid element approach is here chosen as the simulation strategy moving forward.

3.2 Benchmarking software with a reference case

The numerical software available to VBC is benchmarked using a solid element reference case, for which the stress results are known. Both the accuracy of the numerical models, in terms of stress prediction at a certain location, as well as the functionality of the numerical software, is evaluated. The reference case description, model setup and results from the benchmarking simulations are presented in Sections 3.2.1 through 3.2.5 below.

3.2.1 Reference case from previous work

The reference consists of results from previous work by Molker [27]. A brief description the geometry in question, laminate configuration and boundary conditions from the reference is presented below.

The reference consists of a flat composite plate, $30x30x1.5$ mm in size. The plate is modeled with orthotropic laminas, a $[90_2/0_2]_s$ stacking and is subject to displacement boundary conditions on the midplane as well as a distributed static load, acting on the upper surface. Abaqus is used as a solver. A schematic image of the plate can be seen in Figure 3.2, while Equation (3.1) gives the boundary conditions. The reference model employs a $53x53x8$ mesh, where hex elements of equal size are used in−plane, along with a resolution of one element per ply through the thickness of the laminate. Global Coordinate System (GCS) stress results, σ_x, σ_y and σ_z, are known through the thickness of the laminate at $(x, y) = (0, 0)$ [27].

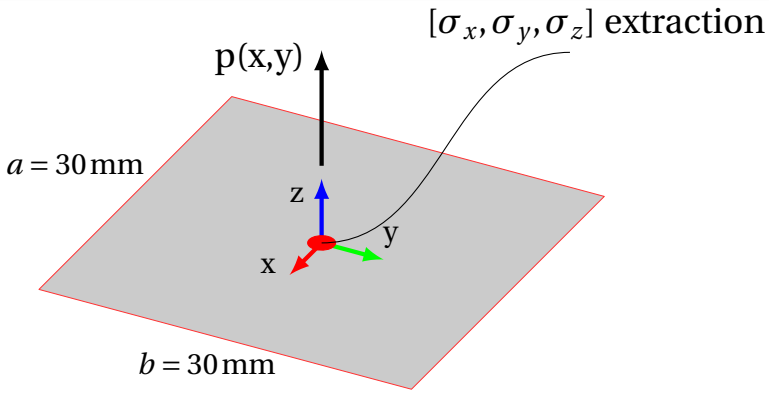

Figure 3.2: Schematic image showing the midplane of the reference plate.

$$\begin{cases} p(x,y) & = p_0\, cos\left(\frac{\pi x}{a}\right) cos\left(\frac{\pi y}{b}\right) \\ p_0 & = 20\,\text{MPa} \end{cases} \qquad \begin{cases} u_x\left(y = \pm\frac{b}{2}\right) = 0 \\ u_y\left(x = \pm\frac{a}{2}\right) = 0 \\ u_z\left(x = \pm\frac{a}{2},\ y = \pm\frac{b}{2}\right) = 0 \end{cases} \tag{3.1}$$

3.2.2 MSC Nastran plate setup

To model a orthotropic material in MSC Nastran, the material card *MATORT* is used, in which nine known elastic parameters are defined, corresponding to Young's moduli, shear moduli and Poisson ratio for the three directions. Laminate properties, such as ply thickness and stacking, are defined using the shell element property card *PCOMP* which in turn is assigned a midsurface in the model.

From this midsurface, solid *CHEXA* elements are generated using a volumization algorithm in the pre processor, where the laminate properties and mesh size of the *PCOMP* shell are taken into account. In this process, the solid elements are given a *PCOMPLS* property and oriented such that the x-axis of the Element Coordinate System (ECS) corresponds to the main fiber direction of the material, while the z-axis corresponds to the out-of-plane direction.

The numerical model is setup for solving in *SOL 101*, a linear static solver, and *SOL 400*, a nonlinear static solver. Stress results for each element are printed to a *.h5*–file, which is the required input for the post processor. To approximate the stress state at the centroid of each element, stress results are calculated as averages over eight adjacent integration point results for each stress component and element respectively.

3.2.3 MSC Nastran plate results

The GCS stress results of the *MSC Nastran SOL 400* solution does not fully coincide with the reference over the full thickness of the laminate, as can be seen in the stress plots of Figure

3.3. Comparing to the reference, it can be noted that the in−plane stress results (σ_x, σ_y) are solved correctly, while the out−of−plane stress (σ_z) for the upper most three plies is not solved correctly.

Regarding software functionality, it is found the model can be solved in *SOL 400*, however not in *SOL 101* since this solver is not compatible with the material card for orthotropic properties, *MATORT*. For the *SOL 400* case, it is found that the post processor interprets certain data in the *MATORT* card as input from the *MAT1* isotropic material card. This makes the post processor unable to read strength properties, which are needed for evaluations of failure criteria.

Blue crosses signify the reference.
Red circles signify the present solution.

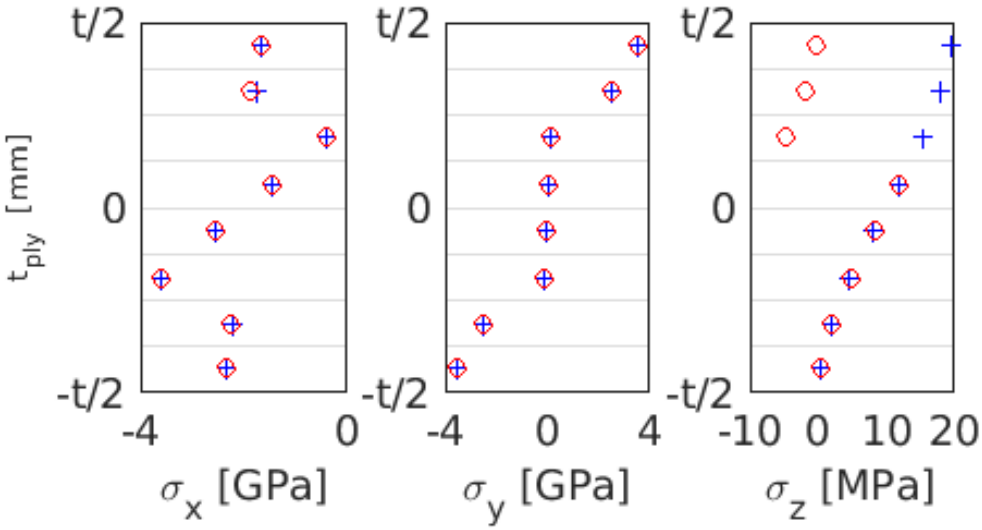

Figure 3.3: GCS stress results at the centre of the plate for the *MSC Nastran SOL 400* solution and the reference.

3.2.4 Abaqus plate setup

The *Abaqus* model is setup similarly to the *MSC Nastran* model described in Section 3.2.2, however with different material and property cards. Here, the material card *MATERIAL* is used, in which orthotropic elastic properties are defined using the *ELASTIC* and *TYPE = ORTHOTROPIC* keywords. The shell type property card *LAMINATE* is used to define the composite laminate properties for the midsurface.

An *ORIENTATION_R* coordinate system is assigned to the *LAMINATE* property and used as a reference coordinate system in the volumization process, which yields one *SOLID SECTION* property per ply. Similarly to the *MSC Nastran* setup, elements are oriented ply-wise in the volumization process, with each respective ECS corresponding to the fiber directions, as described in Section 3.2.2. Solid *C3D8* elements are generated in this process, along with

a *DISTRIBUTION TABLE*, which is a list of element orientations defined from the *ORIENTATION_R* coordinate system.

The load case is controlled using the *STEP* keyword, where both nodal and element centroid results are chosen as field output. For the element results, the option *DIRECTIONS=YES* enables stress results to be output in terms of ECS coordinates, defined by the *DISTRIBUTION TABLE*. All element results, which similarly to the *MSC Nastran* models are averages of adjacent integration point results, are printed to an *.odb*-file that is input to the post processor.

3.2.5 Abaqus plate results

The GCS stress results for the *Abaqus* solution practically coincide with the reference, as can be seen in the stress plots of Figure 3.4. The difference in stress magnitude is less than 1 % at all plies and for all stress components, with the exception of the out-of-plane stress σ_z at the bottom three plies. Here, the difference is slightly larger, however only exceeds 3 % at the bottom ply, where the stress magnitude is close to zero.

Regarding software functionality, it is found that a solid element model with orthotropic material properties can be setup in the pre processor for solving in Abaqus, and that GCS stress results can be read by the post processor. It is further found that ECS results can be used, if the model is setup with a *DISTRIBUTION TABLE* and in such way that one *SOLID SECTION* property per ply is generated during the volumization process. The model is further found to be invariant of how the *ORIENTATION_R* coordinate system is defined.

Blue crosses signify the reference.
Red circles signify the present solution.

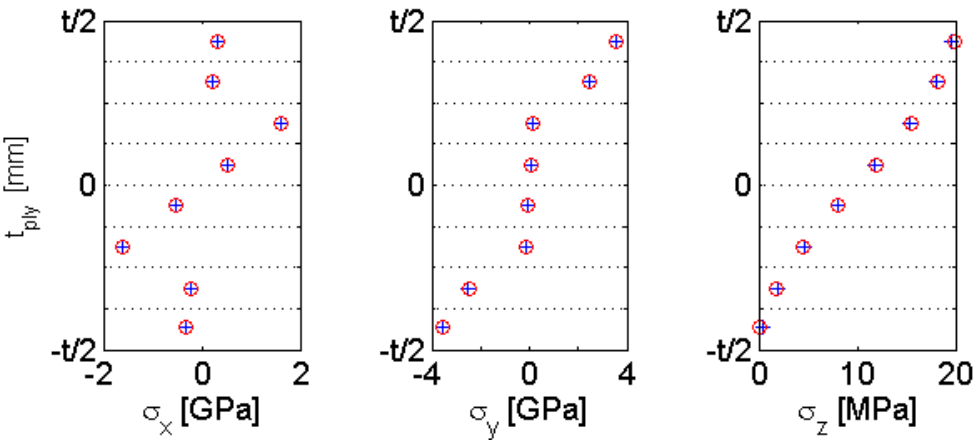

Figure 3.4: GCS stress results at the centre of the plate for the *Abaqus* solution and the reference.

3.3 Numerical models of curved structures

Since the Abaqus solid element model is found to be accurate and functioning with the available software, the construction of models for curved beams is based on using Abaqus as a solver. Here, the setup process further includes defining a set of curved beam geometries subject to evaluation, selecting a load case and determining a required mesh resolution.

3.3.1 Choice of geometries

Two types of curved beam geometries are chosen for the numerical simulations. The first type has a geometrical configuration based on the ASTM standard presented in Section 2.9. This beam type, drawn schematically in Figure 3.5, consists of two straight legs connected by a 90° bend as a single laminate. The second type, drawn schematically in Figure 3.6, consists of two sandwich legs with laminates on top of a foam core, tapering down in a 45° angle to a 90° bend, where the outer and inner laminates are joined together. The two beam types, hereinafter called the *monolithic* and *sandwich* beams respectively, are chosen to represent geometrical features expected in future buses. Two monolithic and three sandwich beam geometries are designed, all of which are 25 mm wide. Laminate properties and additional geometrical features are further presented in Table 3.1.

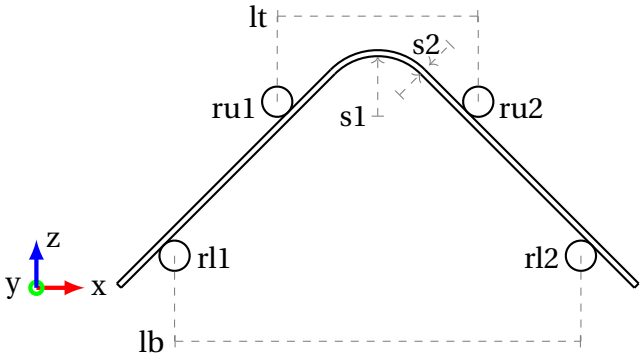

Figure 3.5: Schematic 2D representation of the monolithic beams and the rollers.

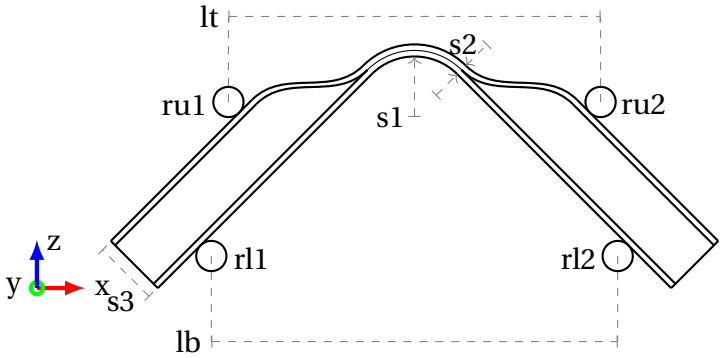

Figure 3.6: Schematic 2D representation of the sandwich beams and the rollers.

Table 3.1: Design parameters for the monolithic and sandwich beams.
* Refers to the total thickness at the curved region.

Name	Layup, one laminate – –	Curve radius s1 mm	Laminate Thickness* s2 mm	Sandwich thickness s3 mm	Upper spacing lt mm	Lower spacing lb mm
MONO6.4 UD	$[0_8]_s$	6.4	3.52	–	75	100
MONO6.4 QI	$[0/45/90/-45]_s$	6.4	1.76	–	75	100
SW30 r11	$[0/45/90/-45]_s$	11	3.52	30	137	181
SW30 r19	$[0/45/90/-45]_s$	19	3.52	30	149	192
SW40 r19	$[0/45/90/-45]_s$	19	3.52	40	149	219

3.3.2 Numerical model setup

The load case for the curved numerical models is designed to resemble the four point bend rig described in Section 2.9. This means that the rollers of the test rig are modelled as friction free rigid bodies, with displacement controlled boundary conditions and surface contact conditions with the beams. Displacement controlled loading of the structures is allowed to continue until a failure criteria is met, as described in Section 3.4.

The rigid body upper and lower rollers, $ru1, ru2$ and $rl1, rl2$ respectively, are given one reference node each on which boundary conditions are asserted. Here, all degrees of freedom (DOF) are fixed, with the exception of translation in the vertical direction for the two upper rollers. The loading imposed through the vertical displacement is controlled by a boundary condition on maximum displacement and a maximum time step in the *STEP* module using the *STATIC* keyword. To avoid rigid body movement of the beams, the DOF associated with lateral translation is further fixed for all nodes located at half the width of the beams. All displacement boundary conditions can be found in Table 3.2. The contact conditions are setup using the *CONTACT* keyword and applied between the surfaces of the laminates and rigid rollers, which are input as *master* and *slave* surfaces respectively.

Table 3.2: Displacement boundary conditions.
* Corresponds to the nodes located at half the width of the beams.

	Translation			Rotation		
DOF	**x**	**y**	**z**	**x**	**y**	**z**
Upper rollers, ru1 & ru2	0	0	free	0	0	0
Lower rollers, rl1 & rl2	0	0	0	0	0	0
Beams*	free	0	free	free	free	free

Similarly to the reference case, a shell midsurface is used in the volumization process to generate solid *C3D8* elements for the composite laminates, to which *C3D8* elements for the foam core materials are connected with node-to-node connections. The composite material

is modelled using the *MATERIAL* card, where keywords *ELASTIC* and *TYPE=ORTHOTROPIC* defines orthotropic behavior. Here, elastic and strength parameters for NCF205, found in Tables 2.1 and 2.2 respectively, are used throughout. With the same material card type, P100 foam is modelled as isotropic and elastic ideal-plastic using keywords *TYPE=ISOTROPIC* and *PLASTIC*. Here, Young's modulus, Poisson's ratios and Maximum Shear Stress limit given in Table 2.3 are the required input. The plastic behaviour is modelled from the Maximum Shear Stress limit. LY556 epoxy material is modelled as isotropic and with linear elastic properties using a Young's modulus of 3.2 GPa and Poisson's ratio of 0.32. This material is used for a matrix enriched region at the junction between the core and upper/lower laminates, as seen in Figure 3.7, which can be expected in a production scenario.

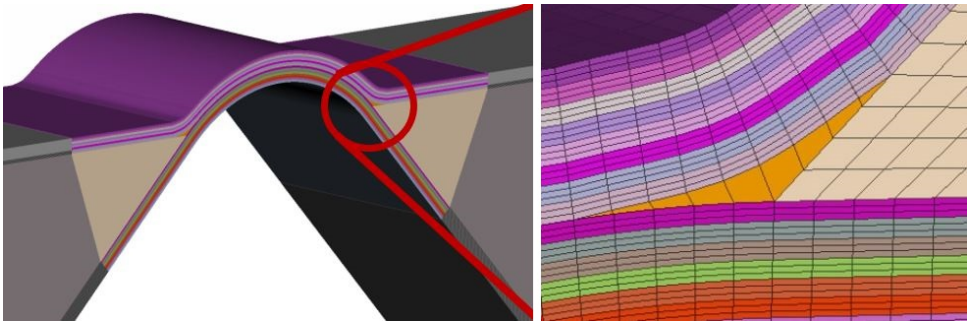

Figure 3.7: Matrix enriched region at the junction between the foam core and upper/lower laminates.

3.3.3 Mesh resolution

The mesh resolution in the region closest to the 90° bend has to be detailed enough to ensure that failure can be predicted with sufficient accuracy, both for the laminates and foam cores. This means that a mesh resolution has to be determined in three directions for the laminates, since this dictates how solid elements within the foam cores can be generated.

The resolution through the thickness of the plies is chosen as three elements per ply, giving 0.073 mm thick elements for 0.22 mm plies, after recommendations by RISE based on studies of similar materials. The resolution along and transverse to the curved section is chosen from a mesh convergence study of a fixed-free cantilever beam, subject to a point load on the free end. Here, the normalized difference in stress magnitude between resolution n and $n-1$, $\Delta\sigma_X$, is studied at half the length of the beam. As can be seen in Figure 3.8, $\Delta\sigma_X$ decreases with an increase in number of elements and is less than 1 % at a mesh resolution of 4000 elements, corresponding to an element length of 0.5 mm. This is chosen as the resolution along the curved structure, while the element length in the transverse direction is chosen as 1 mm, motivated by a lesser need for accuracy.

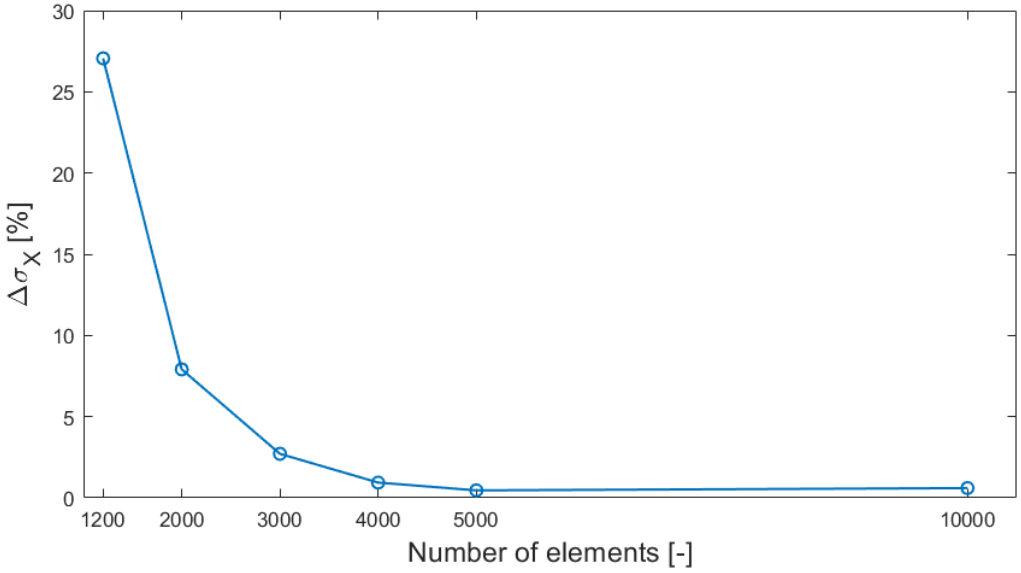

Figure 3.8: Difference in stress magnitude $\Delta\sigma_X$ as a function of number of elements.

3.4 Implementing failure criteria

The numerical software used in the study does not support all failure criteria presented in Section 2.6, so some criteria are implemented through separate scripts, executed in the solving or post processing phases of the simulations. Failure criteria available through native support in the post processing software however include the Maximum Stress and von Mises criteria. These are implemented as scalar result functions and only evaluated for elements of each corresponding material property type, orthotropic composite or foam. The Hydrostatic Criterion is made available in the post processing software as a user generated scalar function that evaluates Equation (2.5) for each solid element with a foam material property. The implementation of LaRC OC is carried out in the solving process using a Fortran script courtesy of Molker et al. [28], which is executed using an Abaqus user variable *UVARM*. Failure of the curved structures is evaluated using the Hydrostatic Criterion and LaRC OC, since the von Mises strength of the modelled foam material is chosen based on assumptions, while Maximum Stress is non-conservative for orthotropic composites (refer Section 2.7.1 and 2.8).

3.5 Physical testing

To verify the simulation methodology, destructive testing of curved composite beams through four point bending is performed at RISE Sicomp (Mölndal, Sweden). Parameters subject to comparison in this process include forces, vertical rig displacements and Principal Strain fields at failure, as well as failure modes and location of first ply failure. The ASTM standard for testing of curved composite beams, described in Section 2.9, is followed throughout. Five individual coupons of six different types are tested. Two coupon types are designed as monolithic laminates without a sandwich core, while four consist of a composite curved section connected to sandwich legs. All parts of the verification process, from the material selection and data recording methods, to discrepancies from the testing standard, are presented in the Section 3.5.1 through 3.5.6, below.

3.5.1 Material selection

Since the destructive testing aims to verify the numerical simulations, materials with similar elastic and strength properties as those modelled are chosen for the coupons. The laminates are made using *NCF 205* fabric infused with *Huntsman LY556 epoxy*, a material that is similar to the previously characterized NCF from which elastic and strength properties are used in the numerical simulations [9].

Due to a limited availability of Divinycell P100 at the time of manufacturing, Divinycell PN115 (PN115) is chosen as core material for the sandwich coupons. PN115 is a PET foam with similar strength and stiffness properties as P100, all of which are presented in Table 2.4. An aspect worth noting with the bulk PN115 available at the time of manufacturing, is that this material contains u-shaped channels, with tracks and holes through the surface and thickness. These channels, which are rectangular and approximately $3x3\text{mm}^2$, are in place to facilitate an even distribution of resin, and can be seen in Figure 3.10a.

3.5.2 Definition of coupon set

The set of six coupon types, presented in Table 3.3, is chosen to represent a wide variety of geometries, with respect to varying curve radii and core thickness. All coupon types are manufactured with a quasi-isotropic (QI) layup, with the exception of *MONO7 UD* which has a uni-directional layup. Eight coupons for each type are manufactured. These are numbered $1-8$ and the five coupons that exhibit the least amount of manufacturing defects upon visual inspection are selected for further use. The monolithic coupons, *MONO7 QI* and *MONO7 UD*, are made with a slightly larger curve radii than for corresponding numerical models, due to a limited availability of jig material at the time of manufacturing.

Table 3.3: Definition of coupon types.
* Refers to the total thickness at the curved region.

Name	Layup, one laminate –	Curve radius mm	Laminate thickness* mm	Sandwich thickness mm	Leg length mm
MONO7 UD	$[0_8]_s$	7	3.52	–	100
MONO7 QI	$[0/45/90/-45]_s$	7	1.76	–	100
SW20 r11	$[0/45/90/-45]_s$	11	3.52	20	165
SW30 r11	$[0/45/90/-45]_s$	11	3.52	30	165
SW30 r19	$[0/45/90/-45]_s$	19	3.52	30	165
SW40 r19	$[0/45/90/-45]_s$	19	3.52	40	165

3.5.3 Manufacturing methods

The manufacturing of test coupons, for which the basic sequence can be seen in the flowchart of Figure 3.9, is performed at RISE facilities in Piteå, Sweden. All coupon types are made using a hand layup technique and vacuum bag resin infusion process, where each type is manufactured as a wide curved plate before individual coupons are cut out.

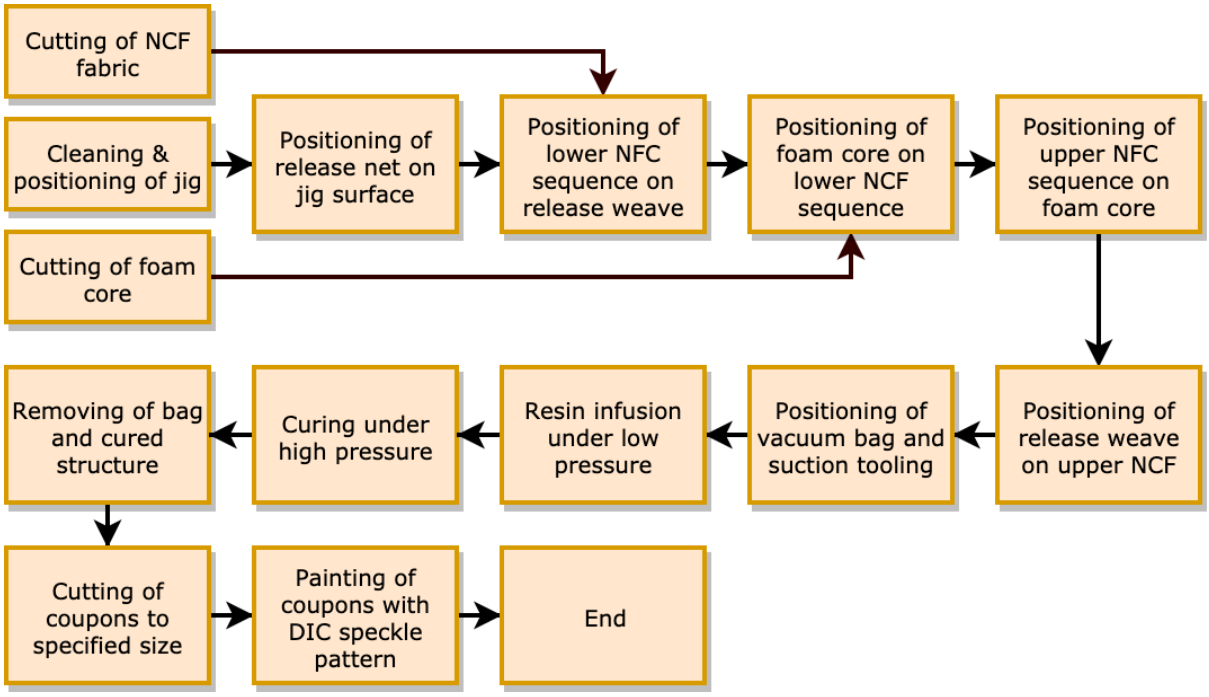

Figure 3.9: Flowchart describing the manufacturing sequence.

In the manufacturing process, all coupon types are made using an infusion pressure of 100 mbar and curing pressure of 600 mbar, with resin and tool temperatures of 40 °C during the infusion. The curing process is initiated 4 hours after the start of the infusion and consists of 4 hours at 80 °C followed by 4 hours at 140 °C. *Airtech Econostitch* release weaves and *Airtech WL 600v* vacuum bags are used throughout, alongside in-house manufactured jigs

and a proprietary mixture of LY556 resin. Figure 3.10 depicts the vacuum infusion process before and after application of the upper sequence and vacuum bag, while Figure 3.11 shows three cut out coupon types. All coupons are primed with white paint and spray painted with a black speckle pattern, used in the digital image correlation (DIC) post processing to obtain the Principal Strain field.

(a) PN115 foam on top of lower NCF sequence. **(b)** Vacuum bag during resin infusion process.

Figure 3.10: Vacuum infusion process.

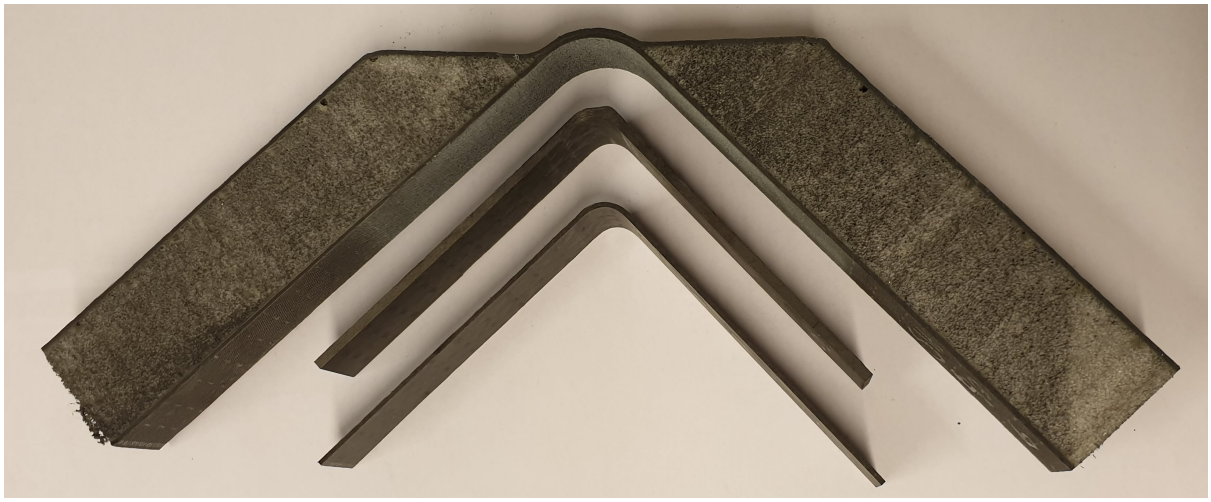

Figure 3.11: Three coupons, cut to the specified width, before speckle pattern painting.

3.5.4 Rig setup and data recording.

The test rig, seen in Figure 3.12, is manufactured according to the ASTM standard described by Section 2.9 and consists of four steel rollers supported by ball bearings on laterally adjustable roller holders, fitted to a Shimadzu electronically controlled hydraulic press. Further equipment includes a DIC camera, external light sources and a computer. The hydraulic press has a *SFL-50KNAG* load cell rated to 50 kN and is controlled through a software

interface, where the force and vertical displacement at the crosshead is recorded. The DIC camera is controlled using *GOM Correlate Software*, a program that post processes video input from the speckle pattern movement to calculate the Principal Strain field on the side of the coupons. The camera is delimited to taking 950 images in one test event, at a maximum recording frequency of 2 Hz.

The roller holders are designed to accommodate larger coupons than proposed by the ASTM standard, in order to fit all coupon types without the risk of clashing. To ensure that the coupons are positioned symmetrically over the crosshead, 3D-printed fitment guides are used for the roller holders. One of these guides can be seen depicted in Figure 3.12b.

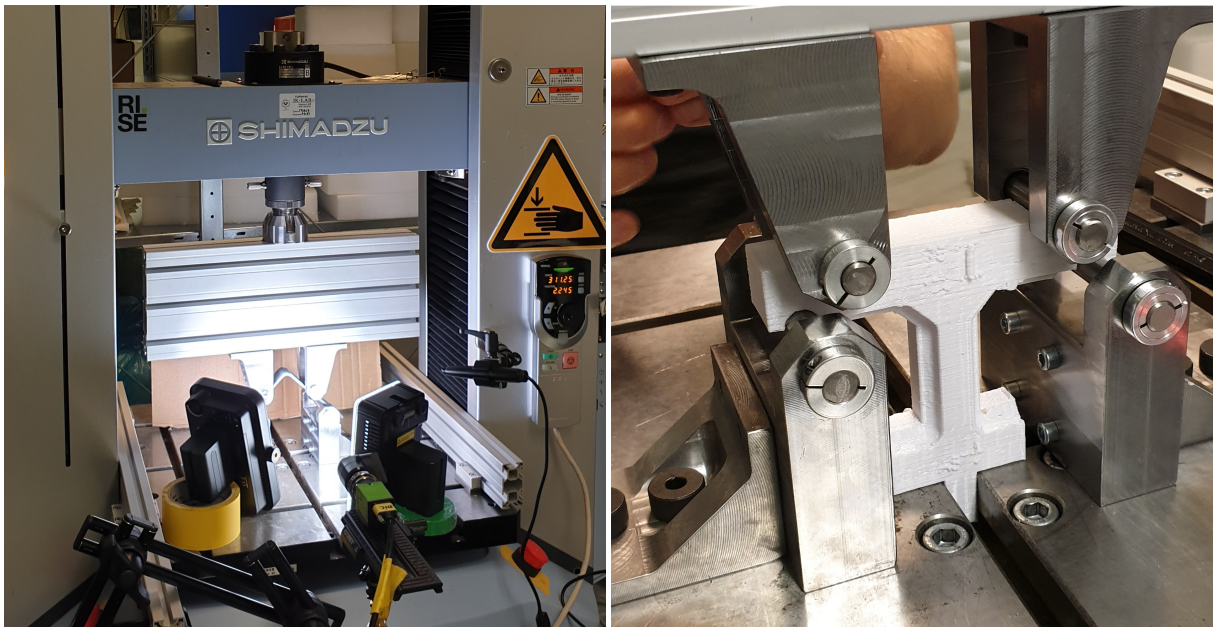

(a) Setup of four point bend rig and DIC camera. **(b)** Fitment guides.

Figure 3.12: Rig setup.

3.5.5 Test protocol

After adjusting the roller placements for a specific coupon type, a coupon is placed centrally in the rig and preloaded to 4 N, to ensure that contact with all rollers is made. During the test, an initial crosshead speed of 0.5 to 1.5 mm/ min and final speed of 0.5 to 3 mm/ min is used. The test is allowed to continue until first ply failure is observed, either through visual inspection or detection of a significant force drop in the force-displacement recordings. After first ply failure is observed, the force-displacement data is extracted, along with photographs of the failed coupon and DIC output as Principal Strain plots.

3.5.6 Discrepancies from the ASTM standard

Since the scope of the study is limited in time and resources, certain discrepancies from the ASTM test standard are deliberately made. These discrepancies, as well as known causes and possible risks, are presented in Table 3.4.

Table 3.4: Discrepancies from the ASTM D6415 test standard.

Discrepancy	**Cause**	**Risk**
Inner radii $\neq 6.4\,\text{mm}$.	Jig material availability and the need for testing different curve radii.	High stiffness, causing improper loading of the curved section.
Laminate thickness $\leq 2\,\text{mm}$.	Thickness determined by material and layup.	Low stiffness in the coupon legs, causing greater rig displacement than recommended by the standard.
Sandwich legs are used.	Sandwich constructions are of interest for the study, while no other applicable ASTM standards are found.	Too stiff legs, causing improper loading of the curved region.
Roller spacing is greater than specified.	Larger coupons than intended by the standard are used.	Clash between rig and coupons or upper and lower roller holders.
Improper use of cutting tools.	Tool availability, lack of water-lubricated precision saw.	Premature failure caused by notched or delaminated coupon edges.
Surface roughness of coupons not measured.	Tool availability and time scope of study.	Premature failure in longitudinal compression, caused by out-of-plane fiber waviness.
Sampling rate of $3-10\,\text{Hz}$ not used.	Sample rate limited to 2Hz by DIC software.	Not possible to capture first ply failure or Principal Strain at a load step right before failure.

4

Results

The following chapter presents results obtained during the numerical simulations and physical testing. For the numerical models, results include figures of the deformed beams, Principal Strain, out−of−plane stress σ_z and failure criteria results at the load step that corresponds to first ply failure. Information on laminate failure parameters, such as failure mode and fiber angle of the failed ply, as well as roller reaction forces and displacements at first ply failure, are further tabulated for each coupon type respectively.

For the physical testing results are, when applicable, given for a representative coupon of a certain coupon type and include images of Principal Strain and failed laminates. Crosshead reaction forces and displacements are further tabulated for load steps that correspond to failure, as well as plotted over the full tests, for each coupon type respectively.

4.1 Numerical simulations of monolithic beams

The following section presents results obtained during numerical simulations of the two monolithic beam models. Results on out−of−plane stress σ_z, Principal Strain, roller reaction force and displacement are given for a load step that corresponds to first ply failure according to LaRC OC.

4.1.1 MONO6.4 UD

The *MONO6.4 UD* model predicts failure at a vertical roller displacement of 1.32 mm according to the Maximum Stress criteria and 1.28 mm according to LaRC OC. The deformed shape at failure according to LaRC OC can be seen in Figure 4.1a, while Figure 4.2 shows the out−of−plane stress σ_z and Figure 4.3 displays the evaluated failure criteria at half the width of the curved section. Figure 4.1b further show the Principal Strain plotted on the surface of the curved section. As shown in Table 4.1, first ply failure occurs in a matrix interface mode, corresponding to out−of−plane delamination, in ply 7 of 16 at the curved section.

Table 4.1: Laminate failure parameters at first ply failure for *MONO6.4 UD* (LaRC OC).

Failed ply -	**Ply angle** °	**Failure mode** -	**Failure angle** α °	**Reaction force** N	**Displacement** mm
7	0	Matrix interface	90	440	1.28

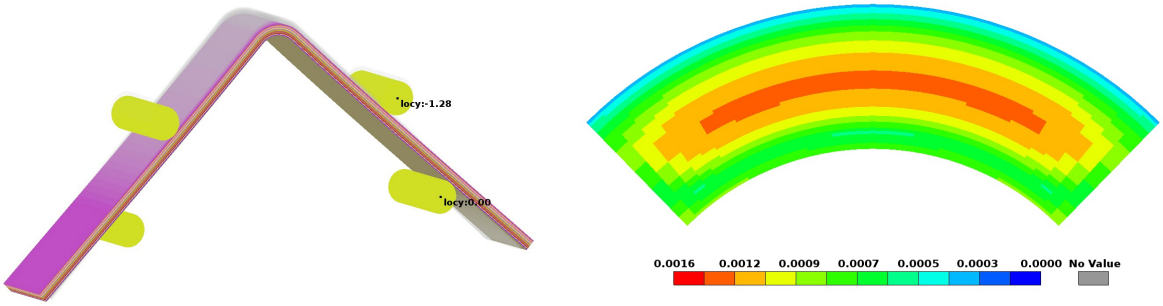

(a) Deformation at failure, with the unloaded position shaded in grey.

(b) Principal Strain plotted on the surface of the curved section.

Figure 4.1: Displacement and Principal Strain at first ply failure for *MONO6.4 UD* (LaRC OC).

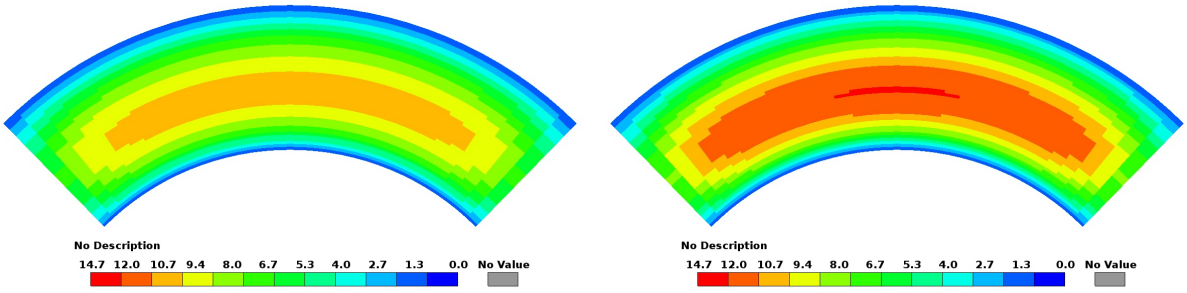

(a) σ_z plotted on the side of the curved section.

(b) σ_z at half the width of the curved section.

Figure 4.2: Out−of−plane stress σ_z at first ply failure for *MONO6.4 UD* (LaRC OC).

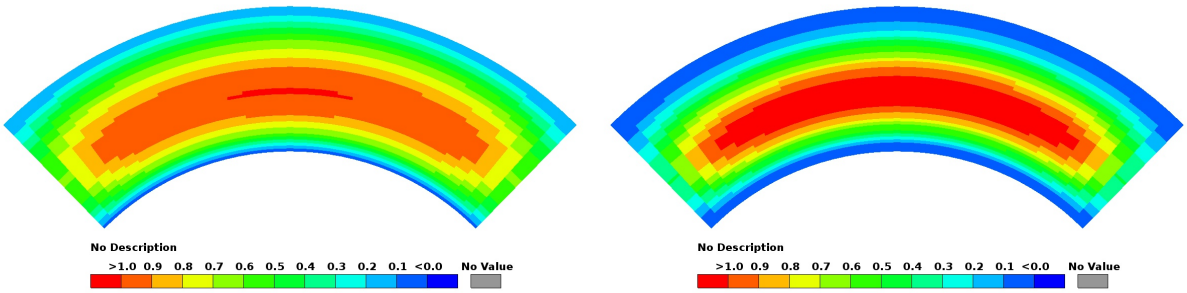

(a) Maximum Stress criterion at half the width of the curved section.

(b) LaRC OC criterion at half the width of the curved section.

Figure 4.3: Failure criteria evaluation for *MONO6.4 UD* (LaRC OC).

4.1.2 MONO6.4 QI

The *MONO6.4 QI* model predicts failure at a vertical roller displacement of 5.8 mm according to the Maximum Stress criteria and 5.6 mm according to LaRC OC. The deformed shape at failure according to LaRC OC can be seen in Figure 4.4a, while Figure 4.5 show the out−of−plane stress σ_z and Figure 4.6 displays the evaluated failure criteria at half the width of the curved section. Figure 4.4b further shows the Principal Strain plotted on the surface of the curved section. As shown in Table 4.2, first ply failure in one ply only is not captured at the displacement load rate used in the present model. Failure in a matrix interface mode, corresponding to out−of−plane delamination, is however found to occur on one load step in plies 3 – 5 of 8 at the curved section.

Table 4.2: Laminate failure parameters at first ply failure for *MONO6.4 QI* (LaRC OC).

Failed plies -	**Ply angle** °	**Failure mode** -	**Failure angles** α °	**Reaction force** N	**Displacement** mm
3-5	90/−45/−45	Matrix interface	90	310	5.6

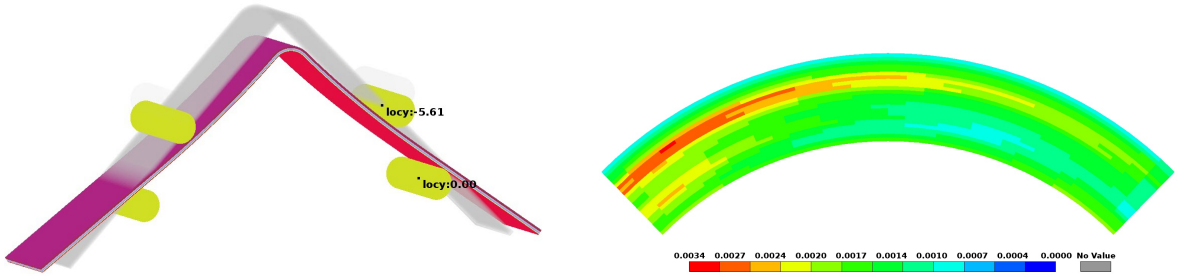

(a) Deformation at failure, with the unloaded position shaded in grey.

(b) Principal Strain plotted on the surface of the curved section.

Figure 4.4: Displacement and Principal Strain at first ply failure for *MONO6.4 QI* (LaRC OC).

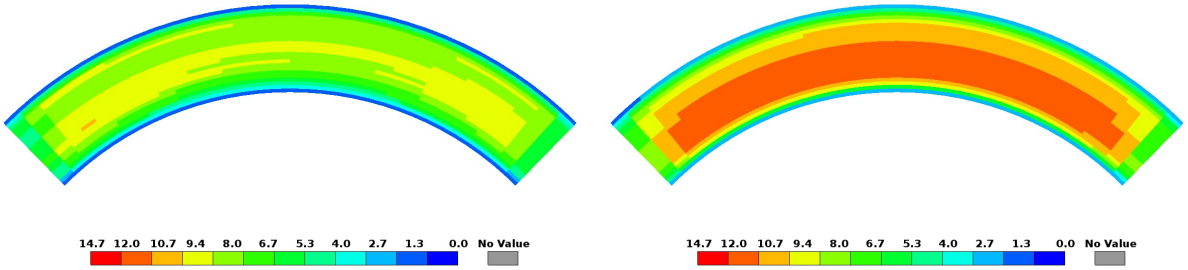

(a) σ_z plotted on the side of the curved section.

(b) σ_z at half the width of the curved section.

Figure 4.5: Out−of−plane stress σ_z at first ply failure for *MONO6.4 QI* (LaRC OC).

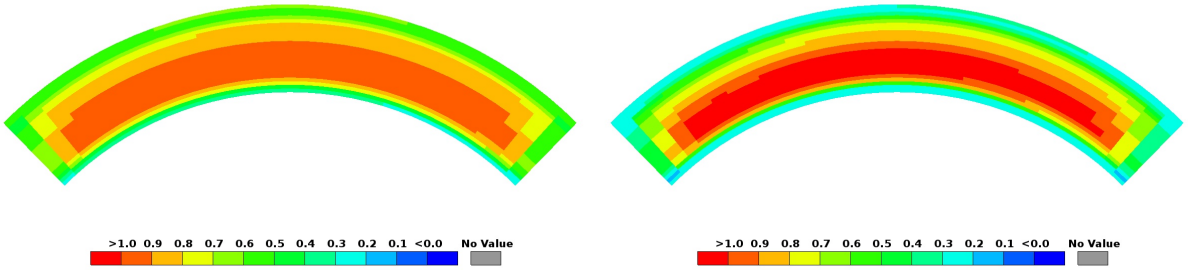

(a) Maximum Stress criterion at half the width of the curved section.

(b) LaRC OC criterion at half the width of the curved section.

Figure 4.6: Failure criteria evaluation for *MONO6.4 QI* (LaRC OC).

4.2 Numerical simulations of sandwich beams

The following section presents results obtained during numerical simulations of the three sandwich beam models. Results are given for the first displacement load step on which either a foam core or NCF failure criteria is exceeded. Foam core failure results are given for both von Mises and Hydrostatic Criterion failure evaluations. Only the Hydrostatic Criterion is however used in the failure evaluation of the beams, as described in Section 3.4.

Common for all three models is that numerical singularities, such as unphysically high stress concentrations, are found to be present at the junction between upper and lower laminates. Given this, along with the limited time scope of the study, the choice is made to disregard results from these elements. Numerical results presented in Sections 4.2.1 through 4.2.3 are thus given without regard to the elements in closest proximity to the junctions.

4.2.1 SW40 r19

The *SW40 r19* model predicts failure in the lower laminate of the curved section, at a vertical roller displacement of 9.1 mm, as shown in Figure 4.8a. The critical element, shown in Figure 4.7, is located in ply 3 of 16 in the curved section, at half the width of the beam. As shown in Table 4.8, failure occurs in an in-plane matrix mode, corresponding to matrix failure within the 90° ply of the lower laminate. Figure 4.8b shows the Principal Strain on the side of the refined section, while Figure 4.9a and 4.9b displays the dominating failure mode and out−of−plane stress respectively, at half the width of the beam. Core failure results, at the load step corresponding to first ply failure, are shown in Figure 4.10a and 4.10b respectively. As can be seen in the latter, the safety factor against core failure, according to the Hydrostatic Criterion, is 3.5.

Table 4.3: Laminate failure parameters at first ply failure for *SW40 r19* (LaRC OC).

Failed ply -	**Ply angle** °	**Failure mode** -	**Failure angle** α °	**Reaction force** N	**Displacement** mm
3	90	In-plane matrix	0	366	9.1

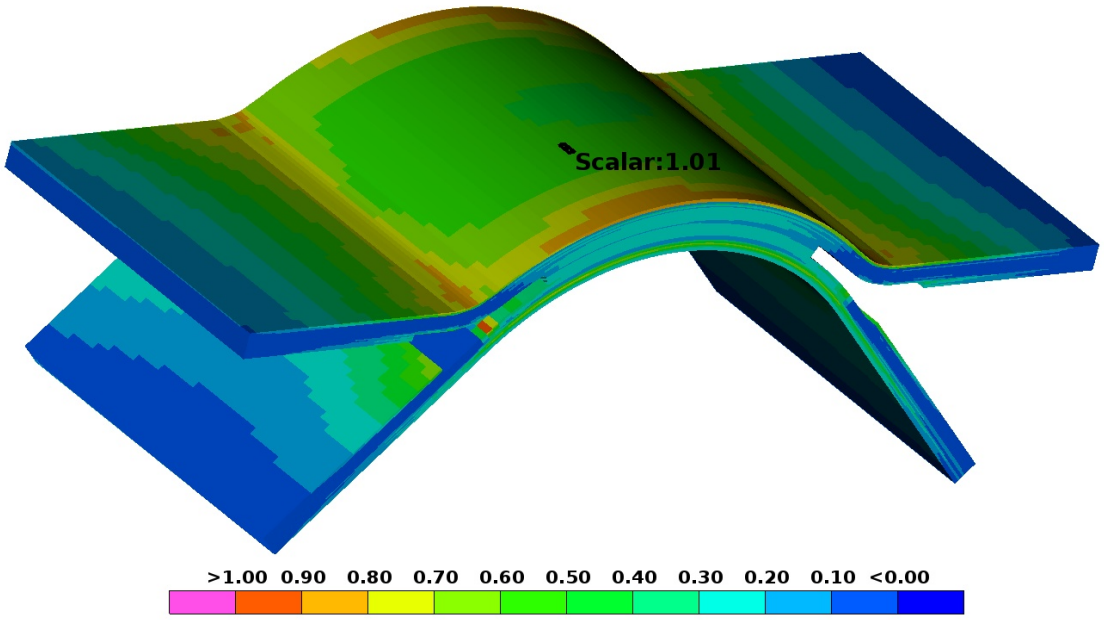

Figure 4.7: Location of the critical element in the *SW40 r19* model (LaRC OC).

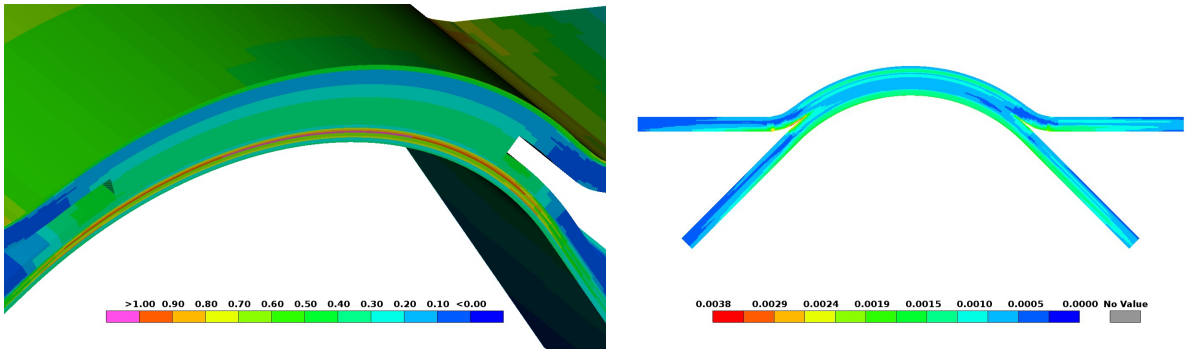

(a) Failure index at half the width of the curved section (LaRC OC).

(b) Principal Strain on the side of the model.

Figure 4.8: Failure index and Principal Strain for the *SW40 r19* model.

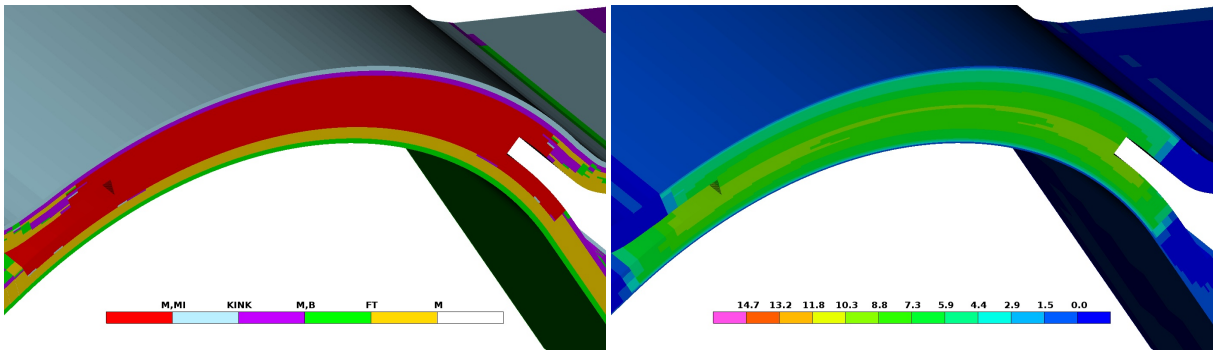

(a) Dominating failure mode at half the width of the curved section (LaRC OC).

(b) σ_z at half the width of the curved section.

Figure 4.9: Dominating failure mode and out−of−plane stress at half the width of the *SW40 r19* model.

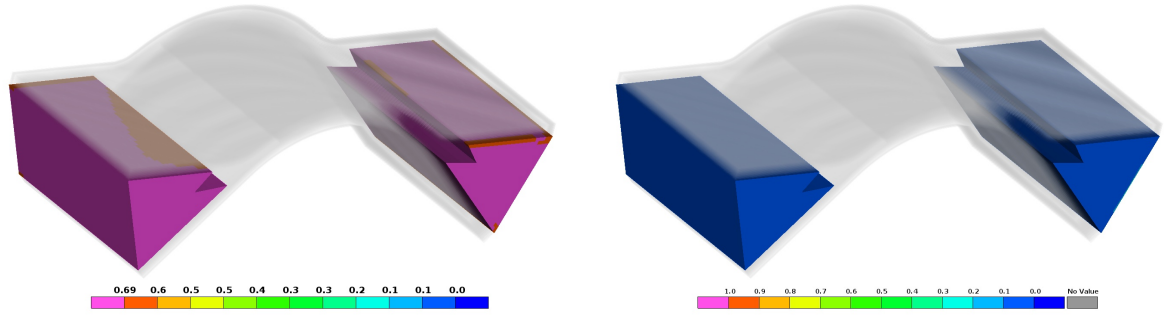

(a) Core failure according to von Mises.

(b) Core failure according to the Hydrostatic Criterion.

Figure 4.10: Core failure predictions for the *SW40 r19* model, at the load step that corresponds to laminate failure (LaRC OC).

4.2.2 SW30 r19

The *SW30 r19* model predicts failure in the lower laminate of the curved section, at a vertical roller displacement of 8.1 mm, as shown in Figure 4.12a. The critical element, shown in Figure 4.11, is located in ply 3 of 16 in the curved section, at half the width of the beam. As shown in Table 4.4, failure occurs in an in-plane matrix mode, corresponding to matrix failure within the 90° ply of the lower laminate. Figure 4.12b shows the Principal Strain on the side of the refined section, while Figure 4.13a and 4.13b displays the dominating failure mode and out−of−plane stress respectively, at half the width of the beam. Core failure results, at the load step corresponding to first ply failure, are shown in Figure 4.14a and 4.14b respectively. As can be seen in the latter, the safety factor against core failure, according to the Hydrostatic Criterion, is 1.6.

Table 4.4: Laminate failure parameters at first ply failure for *SW30 r19* (LaRC OC).

Failed ply -	**Ply angle** °	**Failure mode** -	**Failure angle** α °	**Reaction force** N	**Displacement** mm
3	90	In-plane matrix	0	420	8.4

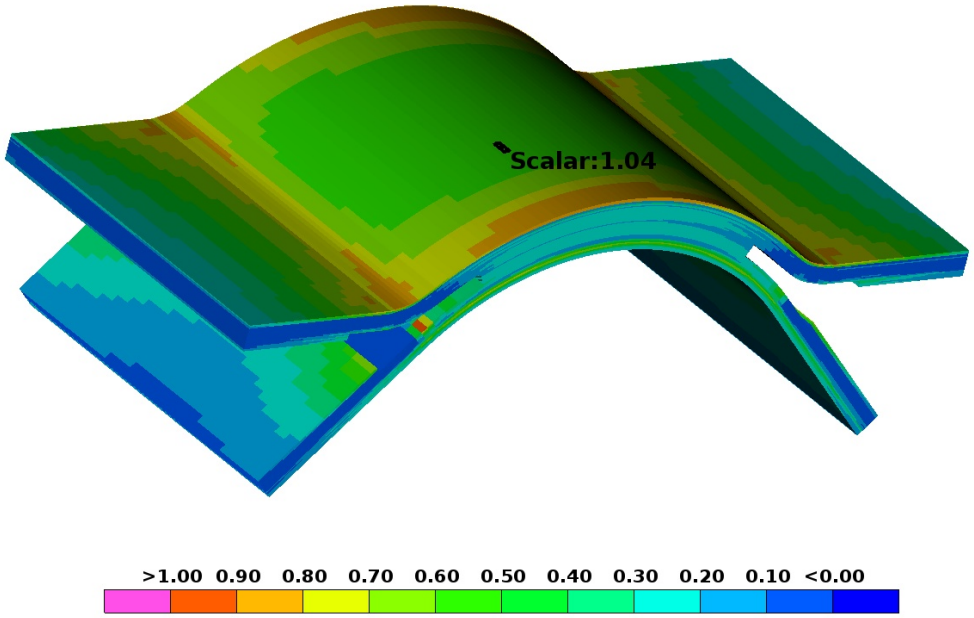

Figure 4.11: Location of the critical element in the *SW30 r19* model (LaRC OC).

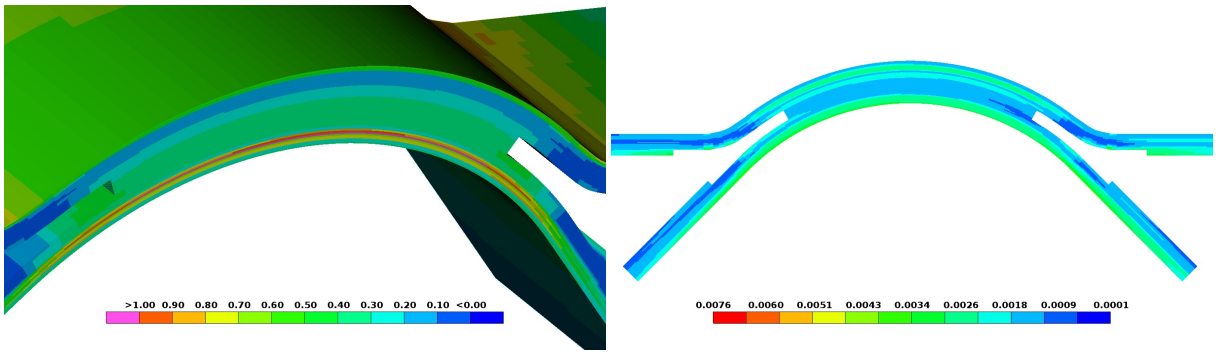

(a) Failure index at half the width of the curved section (LaRC OC).

(b) Principal Strain on the side of the model.

Figure 4.12: Failure index and Principal Strain for the *SW30 r19* model.

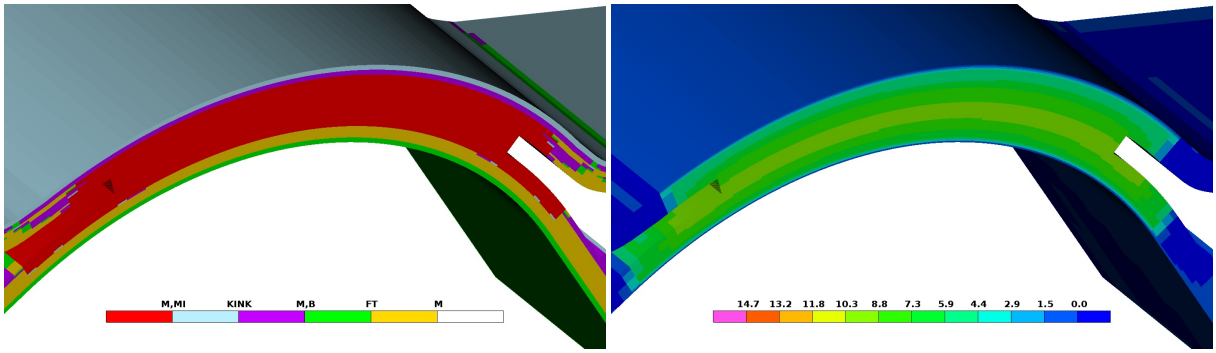

(a) Dominating failure mode at half the width of the curved section (LaRC OC).

(b) σ_z at half the width of the curved section.

Figure 4.13: Dominating failure mode and out−of−plane stress at half the width of the *SW30 r19* model.

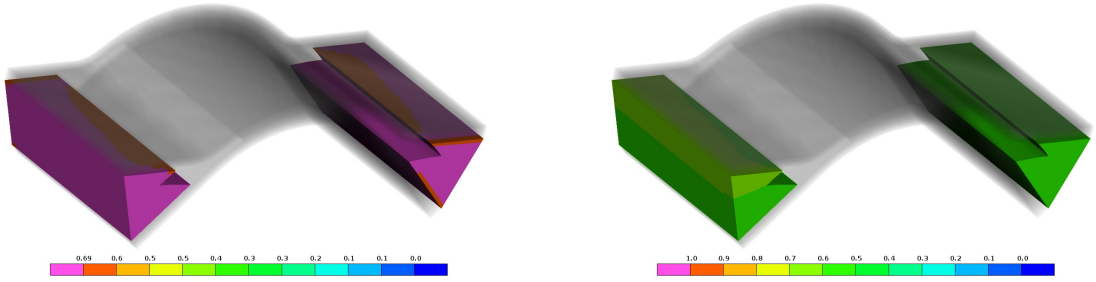

(a) Core failure according to von Mises.

(b) Core failure according to the Hydrostatic Criterion.

Figure 4.14: Core failure predictions for the *SW30 r19* model, at the load step that corresponds to laminate failure (LaRC OC).

4.2.3 SW30 r11

The *SW30 r11* model predicts failure in the lower laminate of the curved section, at a vertical roller displacement of 6.6 mm. The critical element, shown in Figure 4.15, is located on the side of the model in ply 5 of 8 in the lower laminate, under the junction of upper and lower laminates. As shown in Table 4.5, failure occurs in a matrix interface mode, corresponding to a out−of−plane delamination. At this load step, it can be noted that also the 90° ply located in the lower quarter of the curved section is close to failure, as can be seen in Figure 4.17a. Figure 4.16b further shows the Principal Strain on the side of the refined section, while Figure 4.17a and 4.17b displays the dominating failure mode and out−of−plane stress respectively, at half the width of the beam. Core failure results, at the load step corresponding to first ply failure, are shown in Figure 4.18 and 4.18b respectively. As can be seen in the

latter, the safety factor against core failure, according to the Hydrostatic Criterion, is 1.9.

Table 4.5: Laminate failure parameters at first ply failure for *SW30 r11* (LaRC OC).

Failed ply -	**Ply angle** °	**Failure mode** -	**Failure angle** α °	**Reaction force** N	**Displacement** mm
5	-45	Matrix interface	90	360	6.6

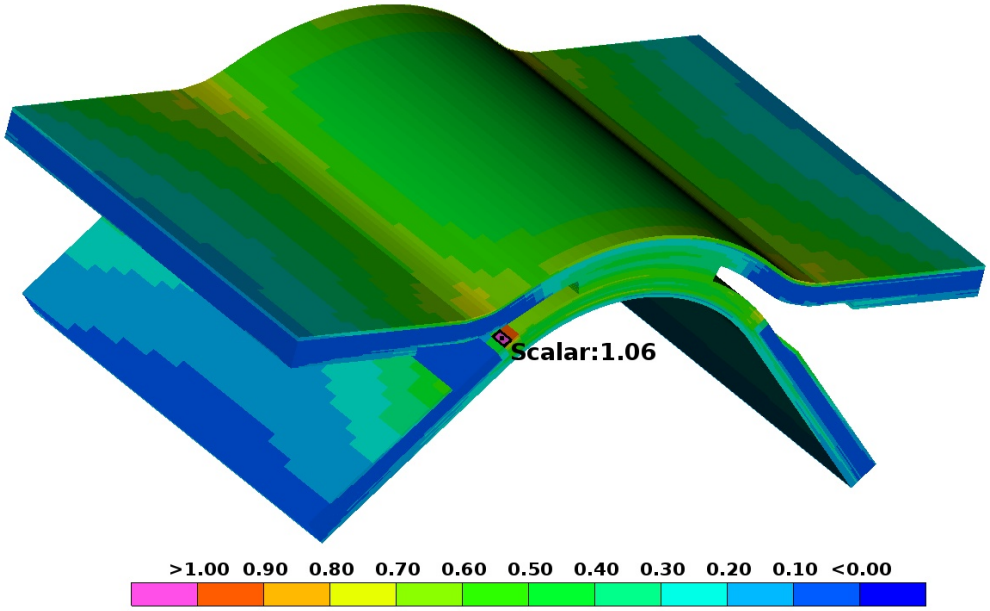

Figure 4.15: Location of the critical element in the *SW30 r11* model (LaRC OC).

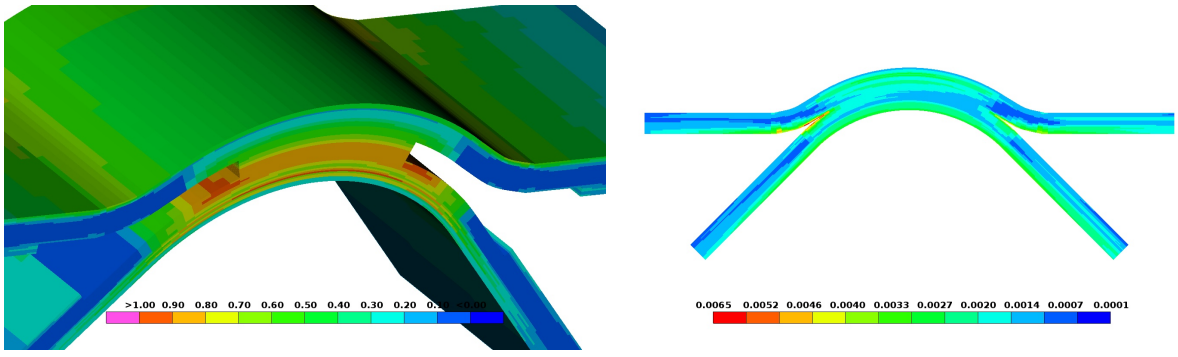

(a) Failure index at half the width of the curved section (LaRC OC).

(b) Principal Strain on the side of the model.

Figure 4.16: Failure index and Principal Strain for the *SW30 r11* model.

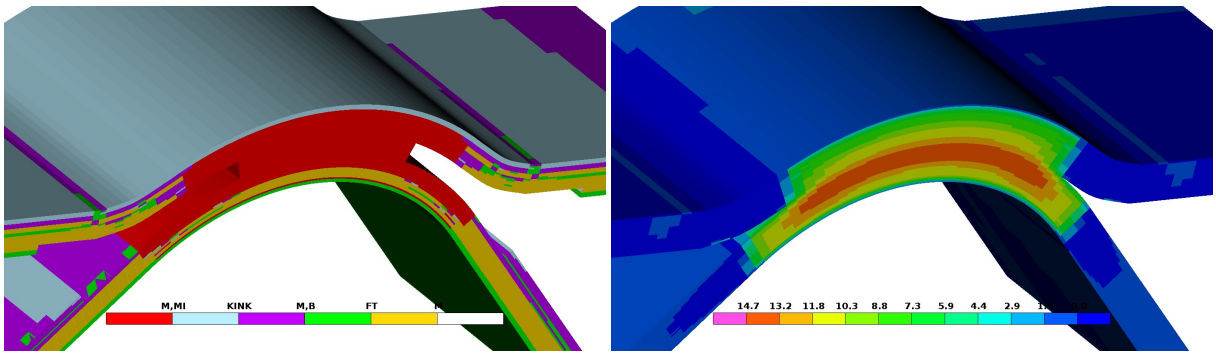

(a) Dominating failure mode at half the width of the curved section (LaRC OC).

(b) σ_z at half the width of the curved section.

Figure 4.17: Dominating failure mode and out−of−plane stress at half the width of the *SW30 r11* model.

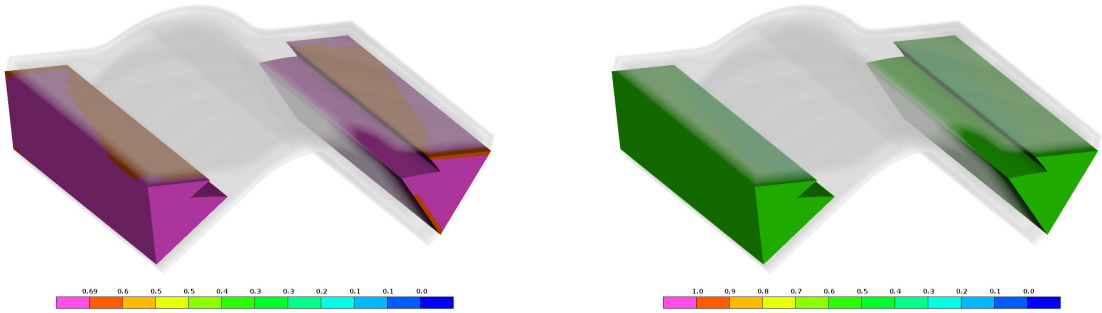

(a) Core failure according to von Mises.

(b) Core failure according to the Hydrostatic Criterion.

Figure 4.18: Core failure predictions for the *SW30 r11* model, at the load step that corresponds to laminate failure (LaRC OC).

4.3 Physical testing of monolithic coupon types

The following section presents results obtained during destructive testing of two monolithic coupon types. Crosshead reaction forces and displacements are tabulated for load steps that correspond to larger delaminations, assumed to be first ply failure, as well as plotted over the full tests, for every coupon of each type. DIC data showing Principal Strain before and after first ply failure is further presented, with delaminations shown circled in red. Because of the relatively low scatter in results for the monolithic coupon types, with regard to reaction forces, displacements and failure types, the DIC data is presented for what is assessed to be a representative coupon for each coupon type.

4.3.1 MONO7 UD

The *MONO7 UD* coupons fail at an average load level of 383 N and vertical crosshead displacement of 2.64 mm, as shown in Table 4.6. Force−displacement data recorded during the full duration of the tests can be seen plotted for all coupons in Figure 4.19.

The five coupons exhibit similar elastic response to the applied loads and first ply failure is observed one quarter into the laminate thickness, roughly corresponding to plies 2 – 5 out of 16. Here, the failure follows the lengthwise direction of the curved section, indicating delamination between plies. The Principal Strain at the last recorded image before first ply failure can be seen in Figure 4.20a, while Figure 4.20b displays the Principal Strain after failure, with the delamination circled in red.

Table 4.6: Forces and displacements at first ply failure for the *MONO7 UD* coupons.

Coupon number	**3**	**4**	**5**	**6**	**7**	**Average**	**Unit**
Force	357	395	399	397	369	**383**	**[N]**
Displacement	2.6	2.6	2.7	2.7	2.6	**2.64**	**[mm]**

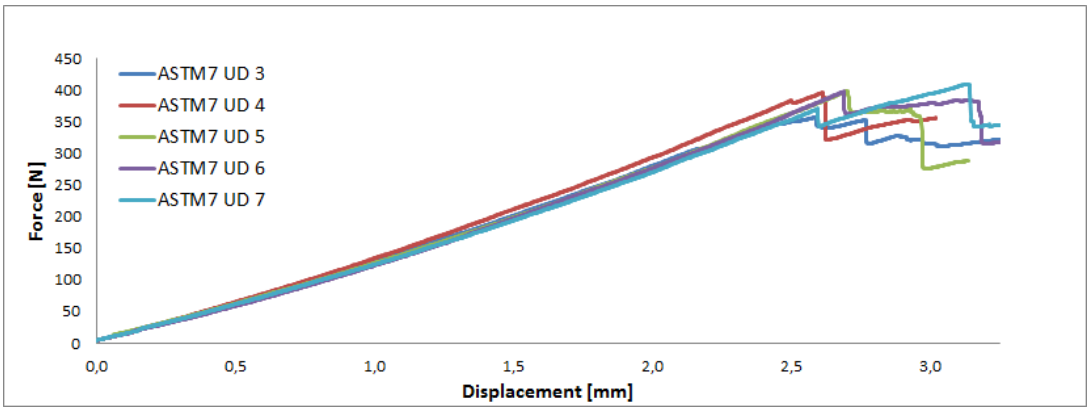

Figure 4.19: Force−displacement plot for the *MONO7 UD* coupons.

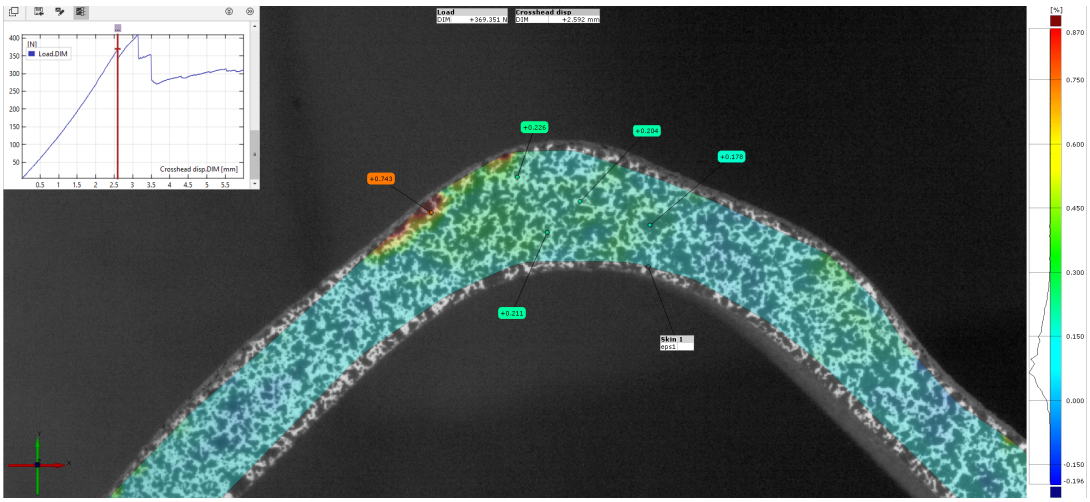

(a) Principal Strain before failure, at 2.5 mm vertical displacement.

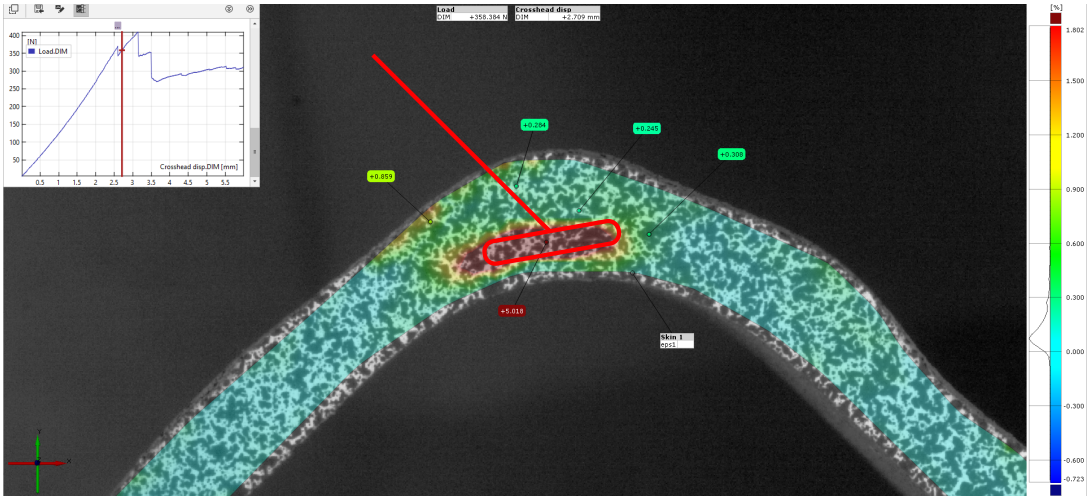

(b) Principal Strain after failure, at 2.6 mm vertical displacement, with the delamination circled in red.

Figure 4.20: Principal Strain for coupon number *7*, representative for the *MONO7 UD* coupons.

4.3.2 MONO7 QI

The *MONO7 QI* coupons fail at an average load level of 262 N and vertical crosshead displacement of 8.68 mm, as shown in Table 4.7. Force−displacement data recorded during the full duration of the tests can be seen plotted for all coupons in Figure 4.21.

The five coupons exhibit similar elastic response to the applied loads and a significant force drop is observed at first ply failure, for most coupons greater than half of the peak load. Here, the failure is found three quarters through the laminate thickness, roughly corresponding to ply 4 – 7 out of 8, as a delamination following the lengthwise direction of the curved section. The Principal Strain at the last recorded image before first ply failure can be seen in Figure 4.22a, while Figure 4.22b displays the Principal Strain after failure, with the delamination circled in red.

Table 4.7: Forces and displacements at first ply failure for the *MONO7 QI* coupons.

Coupon number	**2**	**4**	**5**	**6**	**7**	**Average**	**Unit**
Force	278	293	218	281	237	**262**	**[N]**
Displacement	8.9	9.1	7.7	8.6	8.0	**8.68**	**[mm]**

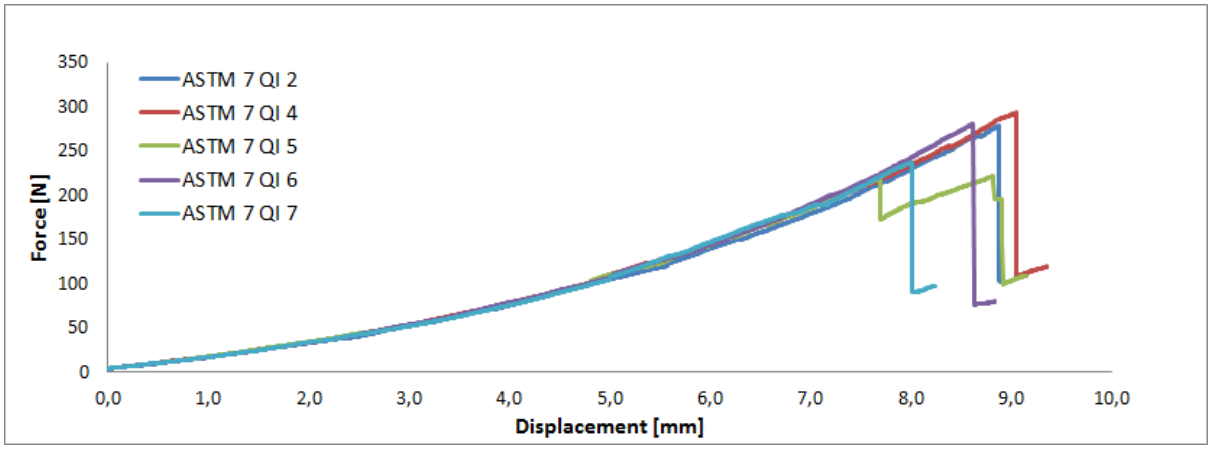

Figure 4.21: Force−displacement plot for the *MONO7 QI* coupons.

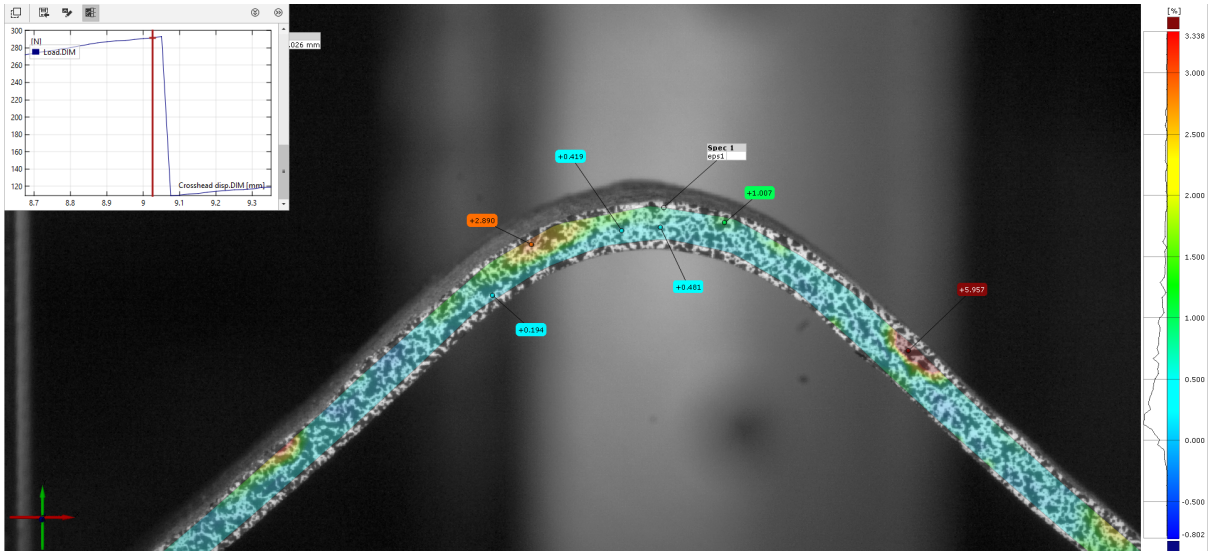

(a) Principal Strain before failure, at 9.0 mm vertical displacement.

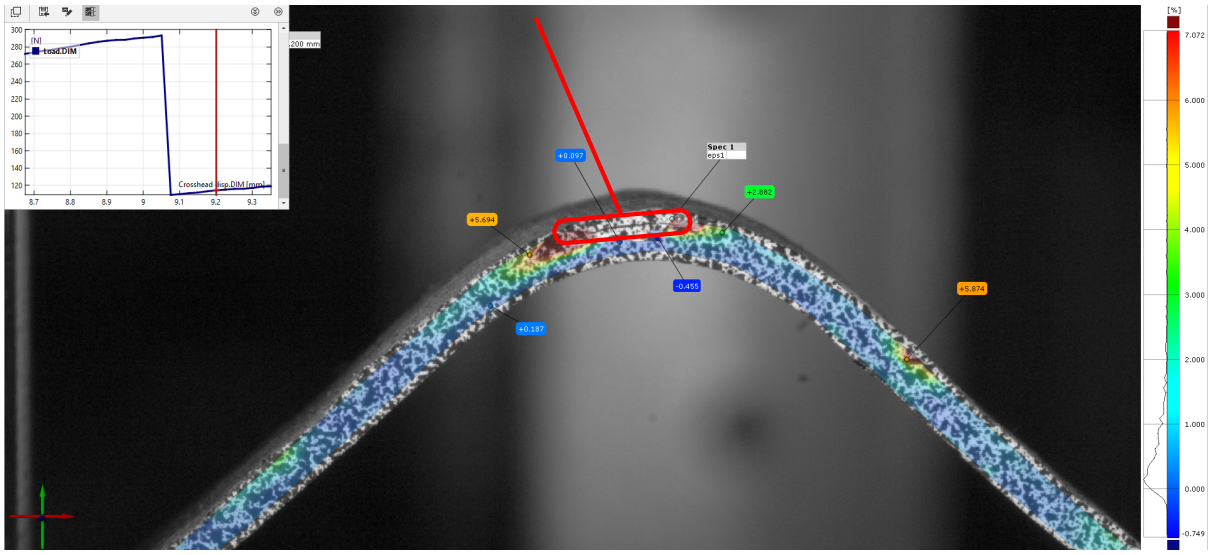

(b) Principal Strain after failure, at 9.2 mm vertical displacement, with the delamination circled in red.

Figure 4.22: Principal Strain for coupon number *4*, representative for the *MONO7 QI* coupons.

4.4 Physical testing of sandwich coupon types

The following section presents results obtained during destructive testing of four sandwich coupon types. Crosshead reaction forces and displacements are tabulated for load steps that correspond to smaller edge delaminations and larger centrally located delaminations,

as well as plotted over the full tests, for every coupon of each type. DIC data showing the Principal Strain is further presented along with snapshots from the recordings showing delaminations. Because of the relatively high scatter in results for the sandwich coupon types, the DIC data is not presented as representative for each coupon type. This data, along with the snapshots showing delaminations, however highlights interesting characteristics in the failure of each coupon type.

4.4.1 SW40 r19

The test event for the *SW40 r19* coupons gives rise to both smaller edge delaminations on the outmost plies of the curved section, as well as larger and more centrally located delaminations at higher load steps. As shown in Table 4.8, edge delaminations are found on four of five coupons, at an average reaction force and displacement of 195 N and 10.3 mm, respectively. The larger delaminations are found in the lower half of the coupons, roughly corresponding to ply $3-8$ of 16. Figure 4.23 displays the force−displacement data recorded during the full duration of the tests.

The edge delamination found in coupon number 7 can be seen circled in red in Figure 4.24a, where also increases in Principal Strain can be seen ahead of the delamination and in the junction between upper and lower laminates. Figure 4.24b further shows the larger centrally located delamination, at a load step beyond tabulated data.

Table 4.8: Forces and displacements at failure for the *SW40 r19* coupons.
* *ED*: Edge delamination
CD: Larger centrally located delamination

Coupon number	**3**	**4**	**5**	**6**	**7**	**Average**	**Unit**
Force, *ED*	200	205	197	N/A	178	195	**[N]**
Displacement, *ED*	10.5	10.6	10.8	N/A	9.3	10.3	**[mm]**
Force, *CD*	266	266	246	287	247	262	**[N]**
Displacement, *CD*	14.3	14.7	14.2	14.7	12.7	14.1	**[mm]**

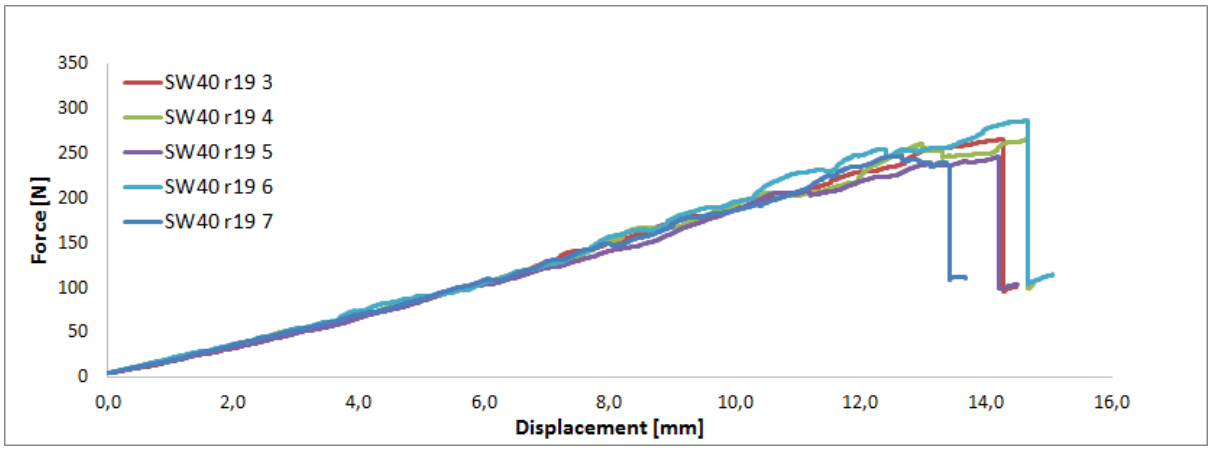

Figure 4.23: Force–displacement plot for the *SW40 r19* coupons.

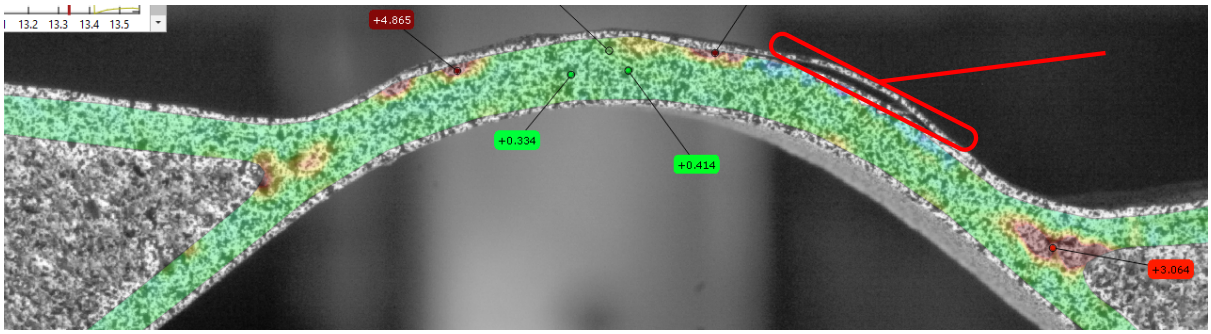

(a) Principal Strain after detection of the first edge delamination, seen circled in red.

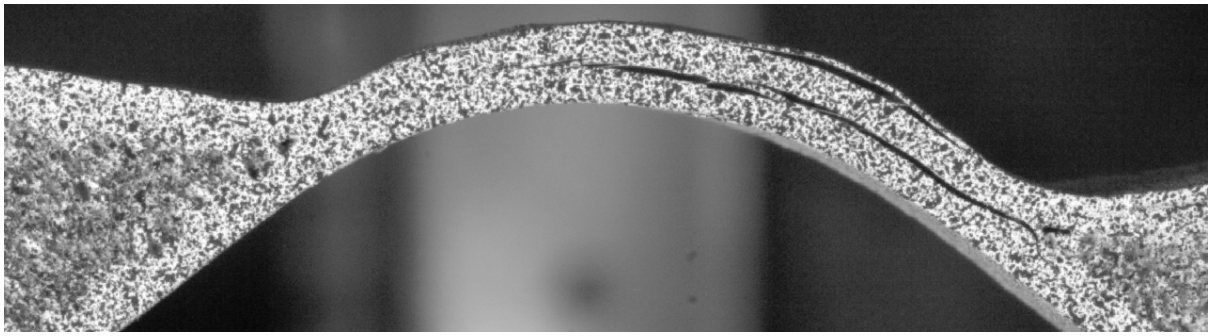

(b) Centrally located delaminations along with edge delaminations for coupon 7 in the *SW40 r19* set.

Figure 4.24: Principal Strain and failure of coupon number 7 in the *SW40 r19* set.

4.4.2 SW30 r19

The test event for the *SW30 r19* coupons gives rise to both smaller edge delaminations on the outmost plies of the curved section, as well as larger and more centrally located delaminations at higher load steps. As shown in Table 4.9, edge delaminations are found on four of five coupons, at an average reaction force and displacement of 243 N and 8.3 mm, respectively. The larger delaminations are found in the lower half of the coupons, roughly corresponding to ply 3 – 8 of 16. Figure 4.25 displays the force–displacement data recorded during the full duration of the tests.

The edge delamination found in coupon number 6 can be seen circled in red in Figure 4.26b, while Figure 4.26a displays the increase in Principal Strain at this position, before failure. An increase in Principal Strain can further be seen in the junction between upper and lower laminates. Figure 4.27 further shows a large centrally located delamination at a load step beyond tabulated data.

Table 4.9: Forces and displacements at failure for the *SW30 r19* coupons.
* *ED*: Edge delamination
CD: Larger centrally located delamination

Coupon number	**2**	**3**	**4**	**5**	**6**	**Average**	**Unit**
Force, *ED*	300	270	175	-	228	243	**[N]**
Displacement, *ED*	10.1	9.4	6.0	-	7.8	8.3	**[mm]**
Force, *CD*	334	280	294	288	326	305	**[N]**
Displacement, *CD*	11.7	9.7	10.0	10.0	11.9	10.7	**[mm]**

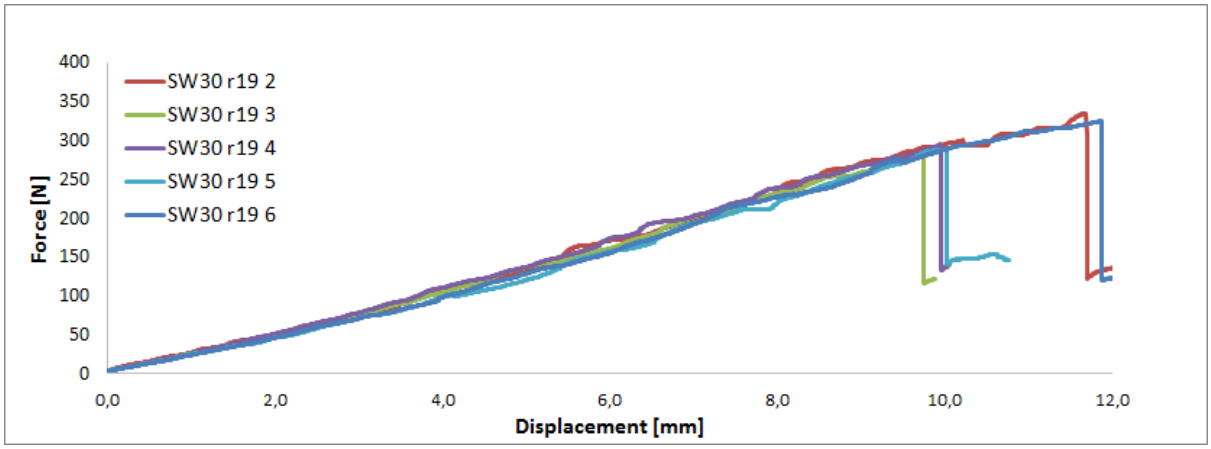

Figure 4.25: Force–displacement plot for the *SW30 r19* coupons.

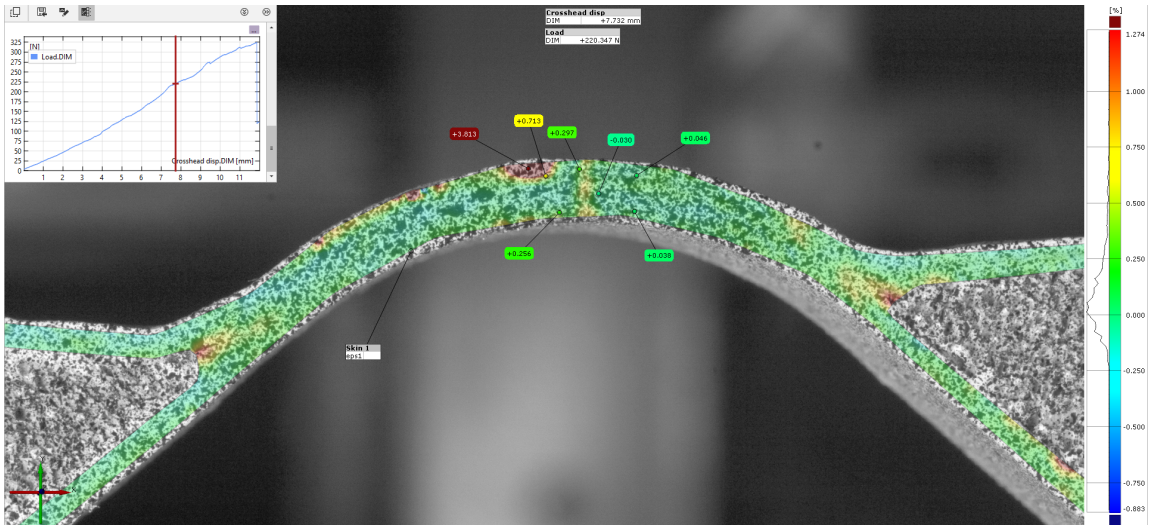

(a) Principal Strain before detection of the first edge delamination.

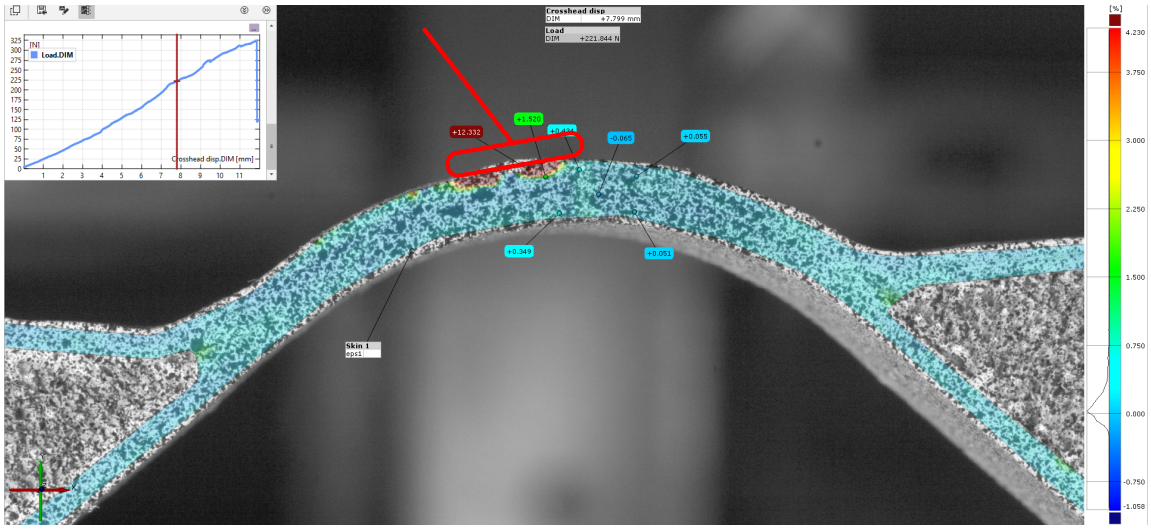

(b) Principal Strain after detection of the first edge delamination, seen circled in red.

Figure 4.26: Principal Strain for coupon number 6 in the *SW30 r19* set.

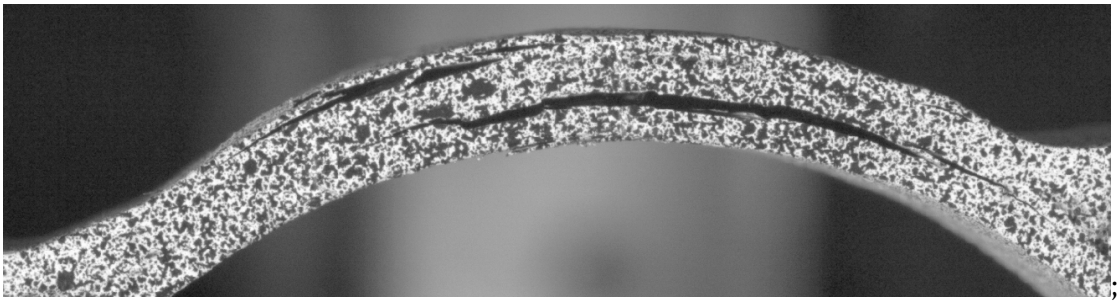

Figure 4.27: Centrally located delaminations along with edge delaminations for coupon 6 in the *SW30 r19* set.

4.4.3 SW30 r11

The test event for the *SW30 r11* coupons give rise to edge delaminations in one case, and more centrally located delaminations in all other cases. As shown in Table 4.10, the edge delamination occurs at a reaction force and displacement of 210 N and 6.7 mm respectively for coupon number 5. Average forces and displacements for the larger delaminations are 255 N and 8.0 mm respectively. The larger delaminations are found in both the lower and upper quarters of the laminate, roughly corresponding to plies 2 – 5 and 12 – 15 of 16. Figure 4.28 displays the force–displacement data recorded during the full duration of the tests.

The edge delamination found in coupon number 5 can be seen circled in red in Figure 4.29b, while Figure 4.29a displays the increase in Principal Strain at this position, before failure. An increase in Principal Strain can further be seen in the junction between upper and lower laminates. Figure 4.30 further shows a large centrally located delamination at a load step beyond tabulated data.

Table 4.10: Forces and displacements at failure for the *SW30 r11* coupons.
* *ED*: Edge delamination
CD: Larger centrally located delamination

Coupon number	**3**	**4**	**5**	**6**	**7**	**Average**	**Unit**
Force, *ED*	-	-	210	-	-	-	**[N]**
Displacement, *ED*	-	-	6.7	-	-	-	**[mm]**
Force, *CD*	265	246	253	262	247	255	**[N]**
Displacement, *CD*	8.3	7.3	8.3	8.0	8.1	8.0	**[mm]**

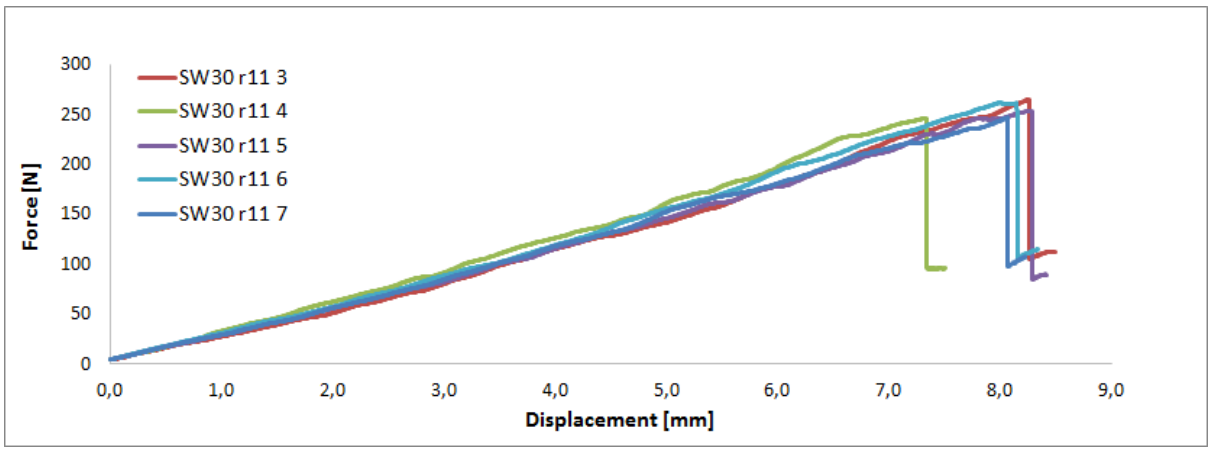

Figure 4.28: Force–displacement plot for the *SW30 r11* coupons.

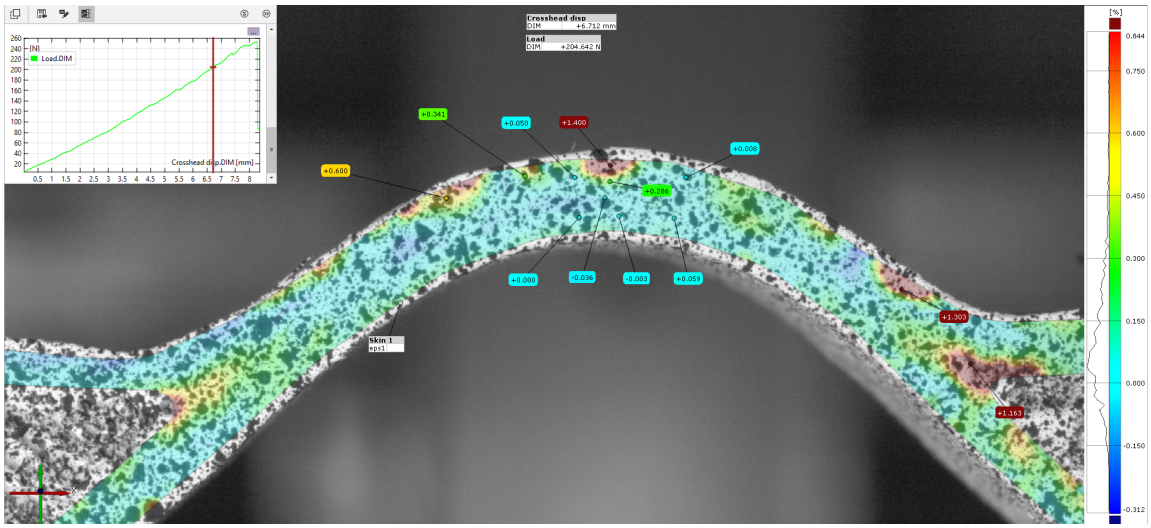

(a) Principal Strain before detection of the first edge delamination.

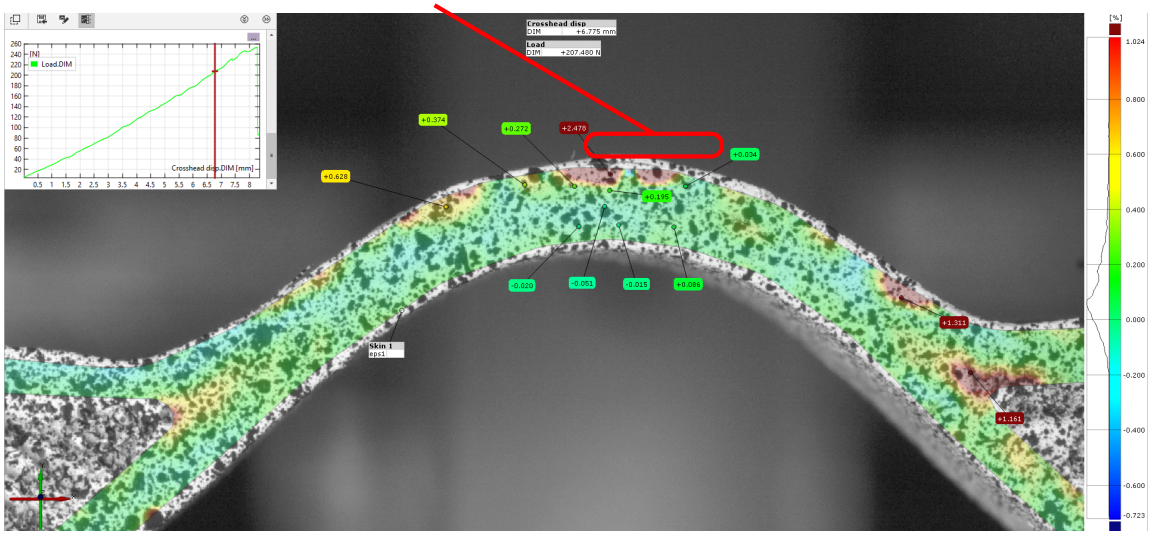

(b) Principal Strain after detection of the first edge delamination, seen circled in red.

Figure 4.29: Principal Strain for coupon number 5 in the *SW30 r11* set.

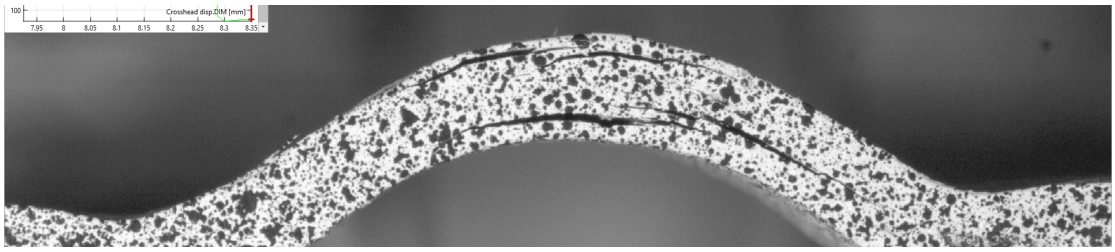

Figure 4.30: Centrally located delaminations along with edge delaminations for coupon 5 in the *SW30 r11* set.

4.4.4 SW20 r11

The test event for the *SW20 r11* coupons gives rise to delaminations in the lower quarter of the curved section, roughly corresponding to plies 2 – 5 of 16, for all five coupons. As shown in Table 4.11, the average reaction force and displacement at failure is 178 N and 4.3 mm respectively. Figure 4.31 shows the force–displacement data recorded during the full duration of the tests and Figure 4.32a displays the Principal Strain before failure. A typical delamination for the present coupon type can be seen circled in red on coupon number 7, in Figure 4.32b.

Table 4.11: Forces and displacements at failure for the *SW20 r11* coupons.
* *CD*: Larger centrally located delamination

Coupon number	**3**	**4**	**5**	**6**	**7**	**Average**	**Unit**
Force, *CD*	162	173	210	169	174	178	**[N]**
Displacement, *CD*	4.1	4.1	4.9	4.3	4.3	4.3	**[mm]**

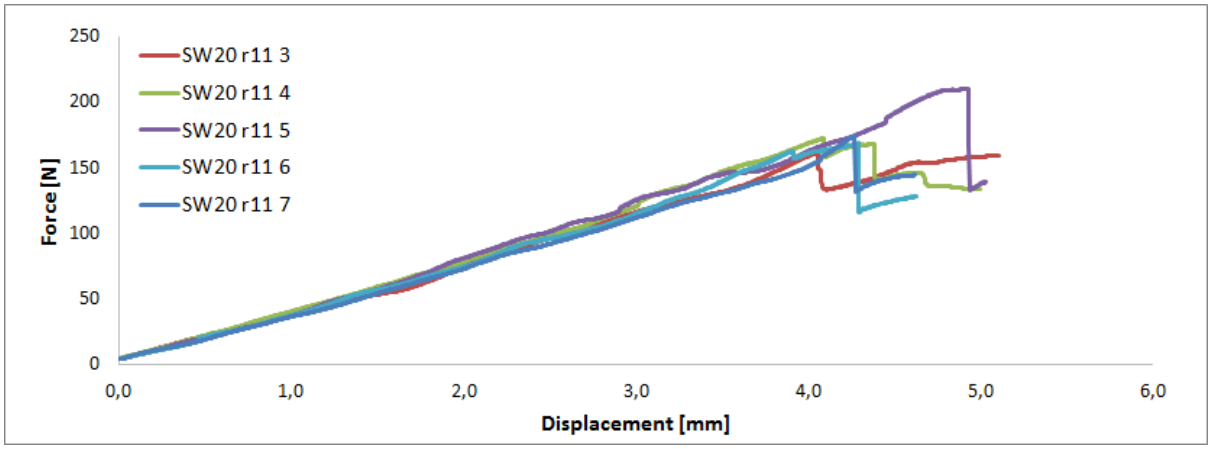

Figure 4.31: Force–displacement plot for the *SW20 r11* coupons.

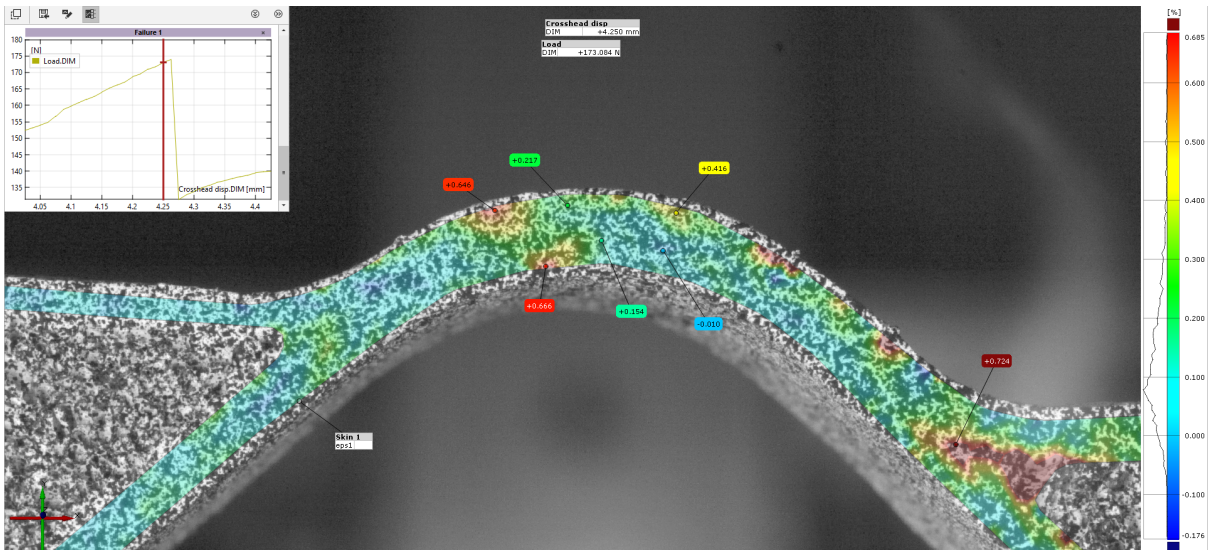

(a) Principal Strain before detection of the first delamination.

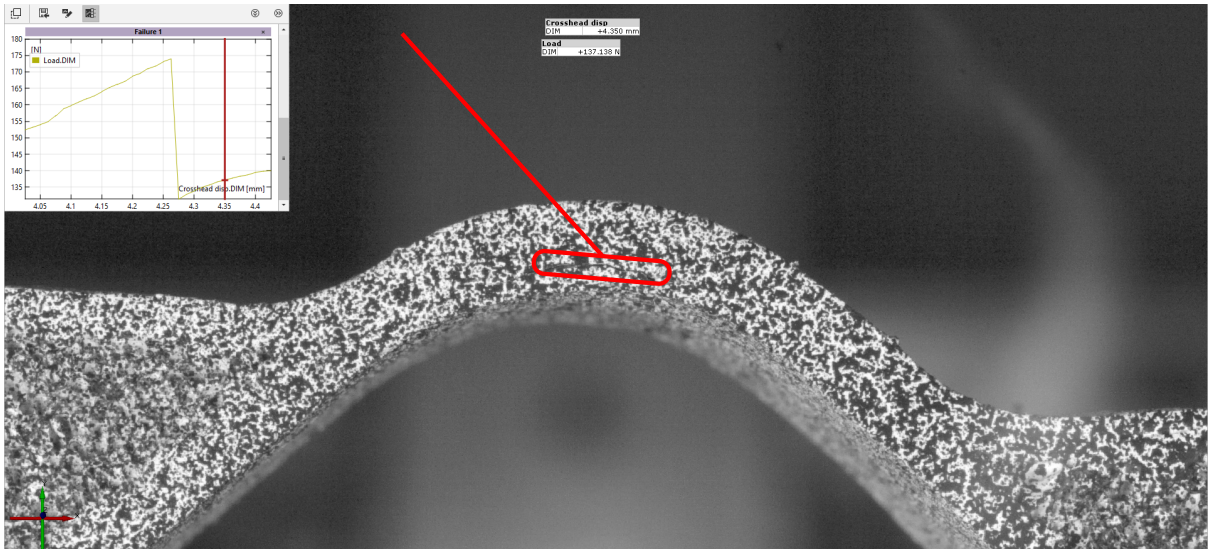

(b) Principal Strain after detection of the first delamination, seen circled in red.

Figure 4.32: Principal Strain and failure of coupon number 7 in the *SW20 r11* set.

5
Discussion

When comparing results from the numerical simulations to the physical testings, some patterns emerge. The numerical models fail at less vertical roller displacement and higher force levels than the corresponding testing coupons, something that may be caused by an overly stiff element formulation and poor aspect ratios. The use of overestimated NCF205 material data in the simulations could also explain this behaviour. While the fiber volume fraction of the manufactured coupons is not measured in the present study, the manufacturing quality could further affect the stiffness of the coupons, with a reduction caused by out−of−plane fiber waviness.

For the *MONO6.4 UD* model, first ply failure is predicted higher up in the laminate than what is observed during physical testing of the *MONO7 UD* coupons. Manufacturing quality could have played a significant role in the failure of these coupons, since the stacking process is found to have been performed such that weft−tows of adjacent plies are placed over each other, introducing large out−of−plane fiber waviness, mainly in the curved section. The *MONO6.4 QI* model predicts out−of−plane delamination failure lower down in the laminate than what is observed for the *MONO7 QI* coupons. This result could be affected by improper loading of the curved section in the coupons, since a thinner laminate than recommended by the ASTM standard is used. It can however be noted that the largest Principal Strain for both the *MONO6.4 QI* model and *MONO7 QI* coupons is found at a position in the laminate that corresponds to the failure on the side of the coupons. Further refining the numerical models to better account for interlaminar stress concentrations on the free edges could thus be an important step towards greater failure prediction accuracy.

The results for the sandwich models are as discussed in Section 4.2 given under the assumption that the unphysically high stresses near the junction between the foam core and upper/lower laminates can be treated as numerical singularities and thus disregarded. Since this region may be affected by manufacturing voids or other defects, it can be argued that this assumption is too non−conservative. None of the tested coupons, in any of the sets, did however show failure initiating in this position, while the prediction of first ply failure location was accurate compared to the larger damages for each respective coupon type. The smaller surface delaminations found on the sandwich coupons could possibly be explained by compressive loading on a region with out−of−plane fiber waviness, also here caused by weft−tows of adjacent plies being stacked on each other.

As for the failure criteria used in the numerical models, the accuracy of the Hydrostatic Criterion can not be considered to be fully evaluated in the present study since the criterion was not triggered in the simulations and no core failure was observed in the physical testing. It is

thus not known if the criterion is applicable for the present material and further evaluations are needed. The criterion is however suitable for use with the available software, since it can be executed automatically in the post processor at a low computational cost and also since it can be used when the von Mises strength of the foam is not known. The LaRC OC criterion is further suitable from an automation perspective, but the implementation through an Abaqus user variable *UVARM* adds considerable computational cost. Since the criterion addresses the lower out−of−plane strength of orthotropic NCF composites it may however be needed in situations where failure prediction of curved composites with high fidelity is important.

While a solid element simulation methodology is presented in the current study, the pre processing work is found to be hard to automate. This is mainly due to the solid element mesh generation process, which is heavily dependant on the shell element midsurface geometry, as well as the volumization algorithm in the pre processor. Defining an automated pre processing methodology that accounts for different geometries and laminate configurations, which also enables results to be output in local fiber directions, is thus found to not be possible under the demarcations set in the study. A further limitation of the presented methodology is that the solid element mesh resolution used in the numerical simulations is computationally costly, limiting the use of solid element models for complete buses.

6

Conclusions and Future Work

The presented solid element simulation methodology provides a starting point for future work on failure prediction of curved composite structures at VBC. In order to meet the demands on accuracy and computational cost, future improvements in challenging areas of the methodology are however needed.

The use of Abaqus as a solver is a step away from commonality that limits VBC from taking advantage of previous modelling experiences related to MSC Nastran. While it can be argued that Abaqus is the most widely used finite element solver for composite structures, a transition to MSC Nastran is needed in this regard. Determining how the available pre and post processors can be used together with MSC Nastran to yield ECS results for orthotropic models is therefore needed in future work.

Investigating modelling techniques that can give accurate failure predictions based on extended use of shell element models is further needed, since the computational cost of only using solid elements for complete buses is too high. This work could include the adaptive node−based modelling technique discussed in Section 3.1, where displacement results from global shell models are connected to local solid element sub models in critical areas. Determining a method for defining the boundaries of the critical areas subject to in−depth analysis would however be needed. Fully transitioning to using shell models in curved composite structures could further be a viable option, by incorporating the in−plane stress result post processing method presented by Rolfes [25]. Further verification work would however be needed to assess if the method could be applicable and accurate enough for sandwich structures.

Ensuring that reliable material data can be used is furthermore a critical step towards accurate failure prediction. Performing coupon level testing may thus be needed in future research to address both the elastic response and failure behaviour of constituent materials. Investigating how the singular behaviour in the junction between the foam core and upper/lower laminates can be resolved using better material models, possibly including progressive damage modelling, may additionally be needed for reliable failure predictions.

Bibliography

[1] N. Hill, "Light weighting as a means of improving heavy duty vehicles' energy efficiency and overall co2 emissions heavy duty vehicles," 2015. [Online]. Available: https://ec.europa.eu/clima/sites/clima/files/transport/vehicles/heavy/docs/hdv_lightweighting_en.pdf

[2] "European commission. 2030 climate & energy framework." [Online]. Available: https://ec.europa.eu/clima/policies/strategies/2030_en

[3] A. Jacob, "BMW counts on carbon fibre for its megacity vehicle," *REINFORCED PLASTICS*, vol. 54, no. 5, pp. 38–41, 2010. [Online]. Available: https://www-sciencedirect-com.proxy.lib.chalmers.se/science/article/pii/S0034361710701739

[4] M. Fagerström, "Lecture notes composite mechanics," Gothenburg, Sweden, 2015.

[5] F. Stig, "An introduction to the mechanics of 3d-woven fibre reinforced composites," 2009. [Online]. Available: https://www.diva-portal.org/smash/get/diva2:211960/FULLTEXT01.pdf

[6] F. T. Peirce, "Geometry of cloth structure," *Journal of the Textile Institute*, vol. 28(3), pp. 45–96, 1937.

[7] D. Mattson, "Mechanical performance of ncf composites," Ph.D. dissertation, Department of Aeronautical and Vehicle Engineering, Luleå University of Technology., Stockholm, Sweden, 2006. [Online]. Available: https://www.diva-portal.org/smash/get/diva2:990288/FULLTEXT01.pdf

[8] D. Wilhelmsson, "Compressive failure of unidirectional ncf composites," Ph.D. dissertation, Department of Industrial and Materials Science, Chalmers Institute of Technology, Gothenburg, Sweden, 2019.

[9] T. Bru, P. Hellström, R. Gutkin, D. Ramantani, and G. Peterson, "Characterisation of the mechanical and fracture properties of a uni-weave carbon fibre/epoxy non-crimp fabric composite," *Data in Brief*, vol. 6, pp. 680–695, 2016. [Online]. Available: https://doi.org/10.1016/j.dib.2016.01.010

[10] H. Molker, "Industrial framework for hot-spot identification and verification in automotive composite structures," Ph.D. dissertation, Department of Industrial and Materials Science, Chalmers University of Technology., Gothenburg, Sweden, 2019. [Online]. Available: https://research.chalmers.se/publication/508484/file/508484_Fulltext.pdf

[11] H. Molker, R. Gutkin, S. Pinho, and L. E. Asp, "Identifying failure initiation in automotive structures made of ncf reinforced composites for hot spot analysis," in *Procedings of 17th European Conference on Composite Materials, ECCM17*, June 2016.

[12] D. Zenkert, *An introduction to sandwich structures*, ser. Student edition, 2005.

[13] "Divinycell p technical data sheet," DIAB Group, Laholm, Sweden.

[14] T. S. Lim, C. Lee, and D. G. Lee, *Journal of Composite Materials*, vol. 38(18), pp. 1639–1661, 2004.

[15] L. J. Gibson and A. M.F., *Cellular solids – structure and properties*. Oxford: Pergamon Press, United Kingdom, 1988.

[16] M. S. Rajput, M. Burman, J. Köll, and S. Hallström, "Compression of structural foam materials – experimental and numerical assessment of test procedure and specimen size effects," *Journal of Sandwich Structures and Materials*, vol. 21(1), pp. 260–280, 2017.

[17] "Divinycell technical data sheet," DIAB Group, Laholm, Sweden.

[18] B. Sundström, *Handbok och formelsamling i Hållfasthetslära*. Stockholm, Sweden: Institutionen för hållfasthetslära KTH, 1998.

[19] S. Abrate, "Criteria for yielding or failure of cellular materials," *Journal of Sandwich Structures and Materials*, vol. 10(1), pp. 5–51, 2008.

[20] W. S. Tsai and E. M. Wu, "A general theory of strength for anisotropic materials," *Journal of Composite Materials*, vol. 5, pp. 58–79, 1971.

[21] S. Pinho, R. Darvizeh, P. Robinson, C. Schuecker, and P. Camanho, "Material and structural response of polymer-matrix fibre-reinforced composites," *Journal of Composite Materials*, vol. 46(19-20), pp. 2313–2341, 2012. [Online]. Available: https://doi.org/10.1177/0021998312454478

[22] H. Molker, D. Wilhelmsson, R. Gutkin, and L. E. Asp, "Orthotropic criteria for transverse failure of non-crimp fabric-reinforced composites," *Journal of Composite Materials*, vol. 50(18), pp. 2445–2458, 2016. [Online]. Available: https://doi.org/0.1177/0021998315605877

[23] S. Pinho, C. Dávila, P. Camanho, L. Iannucci, and P. Robinson, "Failure models and criteria for frp under in-plane or three-dimensional stress states including shear non-linearity," 3 2005.

[24] *ASTM D 6415, Standard Test Method for Measuring the Curved Beam Strength of a Fiber-Reinforced Polymer-Matrix Composite*, ASTM International Std., 2007.

[25] R. Rolfes, K. Rohwer, and M. Ballerstaedt, "Efficient linear transverse normal stress analysis of layered composite plates," *Computers and Structures*, vol. 68, pp. 643–652, 1998.

[26] C. Möller and O. Sundlo, "Method for merging scales in finite element analyses," Master's thesis, Chalmers University of Technology, Gothenburg, Sweden, 2017.

[27] H. Molker, R. Gutkin, and L. Asp, "Hot spot analysis in complex composite material structures," *Composite Structures*, vol. 207, pp. 776–787, 2019.

[28] H. Molker, R. Gutkin, and L. E. Asp, "Implementation of failure criteria for transverse failure of orthotropic non-crimp fabric composite materials," *Composites Part A: Applied Science and Manufacturing*, vol. 92, pp. 158–166, 2016. [Online]. Available: https://doi.org/10.1016/j.compositesa.2016.09.021